POLITECNICO DI TORINO

Master's Degree in
MECHANICAL ENGINEERING

Master's Degree Thesis

Triboelectric harvester for sensor system in smart tires

Supervisors

Prof. EUGENIO BRUSA

Prof. PETER FOLKOW

(Chalmers University of Technology)

Candidate

MATTEO MOSCUFO

DECEMBER 2022

Abstract

The point where a car meets the ground and provides force and isolation is the tire. Estimation, sensing, and power harvesting are the three main areas of research in the field of tire condition monitoring systems (TCMS). The implementation of intelligent tires is highly advantageous for the reduction of disastrous accidents, CO_2 and noise emissions, and also fuel consumption. Sensors mounted on the wheel hub can be used to measure longitudinal, lateral, and vertical tire forces, and pressure but available wheel transducers are expensive, hard to calibrate, and require large space; thus, they are not used for production vehicles. In-depth multidisciplinary research in areas including vehicle dynamics, control, estimate, energy harvesting, and even nanotechnology has been stimulated by the ambition to use intelligent tires. Triboelectric nanogenerators are a promising technology for converting mechanical energy from the ambient environment into electric energy. Via contact electrification and electrostatic induction, these triboelectric nanogenerators, commonly shortened into TENGs, convert mechanical energy from the environment, in this case from the bending and vibration of the tire, into electric energy. The great adaptability of the design shown by TENGs further enhances their ability to convert mechanical energy into electric energy at high conversion efficiencies. Furthermore, they have the great advantage to be lightweight, and easy to produce and they can be built from a large array of materials, which means that potentially they can also be very cost-effective. TENG can be applied also for wearable electronic devices and the Internet of Things (IoT), without the need for an external battery or connecting cables.

The Energy ECS is a comprehensive three-year plan that creates innovative and clean energy solutions for smart mobility and the transition to a greener energy economy. Designing a self-powered sensor system that gathers energy from the environment is one of the goals. The aim of this thesis is to simulate and design a prototype for a flexible triboelectric energy harvester for tire sensors. The first step is applying FEM (COMSOL Multiphysics) for the simulation of the harvester, modeling its mechanical and electric behavior, and MATLAB for data analysis. The second step is building and testing the TENG harvesters at the RISE labs and Nokian tyres, a Finnish company of tire manufacturing.

Contents

List of Figures

Chapter 1

An overview of triboelectric nanogenerators

1.1 The triboelectric effect

The triboelectric effect is a type of charge transfer by which any two materials, after contact with each other, become electrically charged in opposite signs. We may test this phenomenon in daily life by rubbing a plastic rod on a cloth of practically any common fabric, such as animal fur **Fig.1.1**, cotton, wool, polyester, or a combination of fabrics found in contemporary clothes. When it comes close to a sheet of paper, an electric pen like that would easily attract and pick it up. Additionally, a pen of this type will bounce any other electrified pens or objects made of the same substance. The delicate setup of suspending both pens from threads and placing them close to one another makes it simple to identify this repulsion. Such investigations easily support the hypothesis of two forms of measurable electric charge, one of which is essentially its opposite, with the overall charge determined by a sum that takes sign into account. For instance, the temporary charge separation (electric polarisation or dipole moment) of electric charges within the paper is what causes the charged plastic pen's electrostatic attraction to neutral, uncharged sheets of paper. A net force then develops as a result of the dipole's closer charges being drawn to the pen's nonuniform field from a distance more strongly. The little pieces of paper would temporarily polarise in a homogeneous electric field, such as between parallel capacitor plates, but there would be no net attraction. Depending on the materials, surface roughness, temperature, strain, and other characteristics, different polarities and strengths of

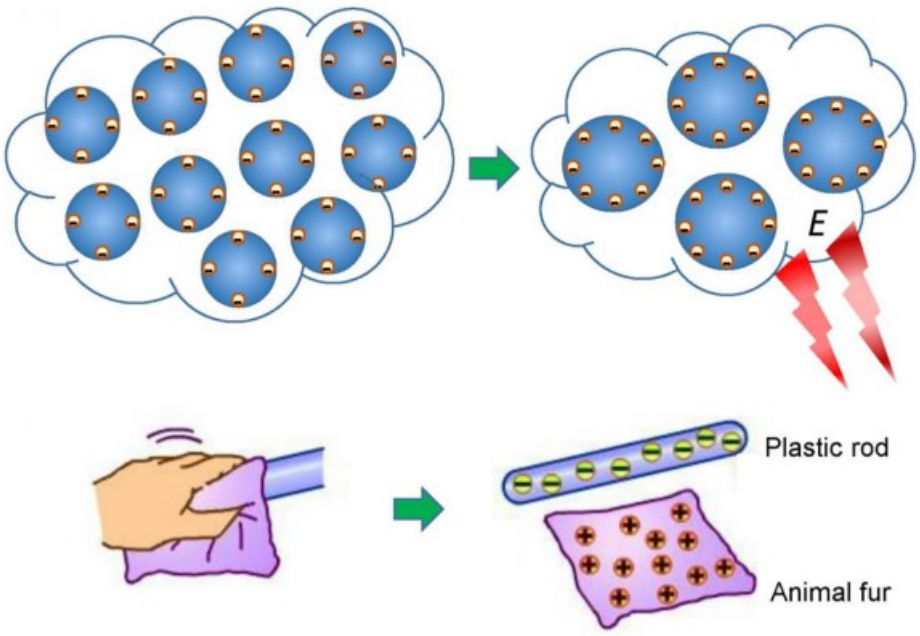

Figure 1.1: An example of a common triboelectrification.[1]

the charges are generated. Because of how unpredictable the triboelectric effect is, only broad generalizations can be derived. Although the triboelectrification effect is known for thousands of years, a fundamental understanding about it is rather limited. Research has been conducted to characterise the triboelectrification process using various methods; however, these methods either lack an accurate control of the electrification process and/or cannot directly reveal the triboelectric interface, thus hardly achieving a quantitative understanding about the triboelectric process.

Most of the research on the triboelectric effect was much more concentrated on the triboelectrification between solid-solid contact than that in non-solid-based triboelectrifications such as between solid-liquid, solid-gas, and liquid-gas contact. However, even in solid-solid triboelectrification, it is not precisely known which charge species transfer during the triboelectrification, especially between nonionic insulator contacts. This lack of knowledge has led to controversy regarding the design of materials for TENGs utilizing solid-solid contacts [2].

Since this discovery, there have been numerous attempts to find a universal pattern of triboelectricity between different materials in an effort to ascertain the precise mechanism.

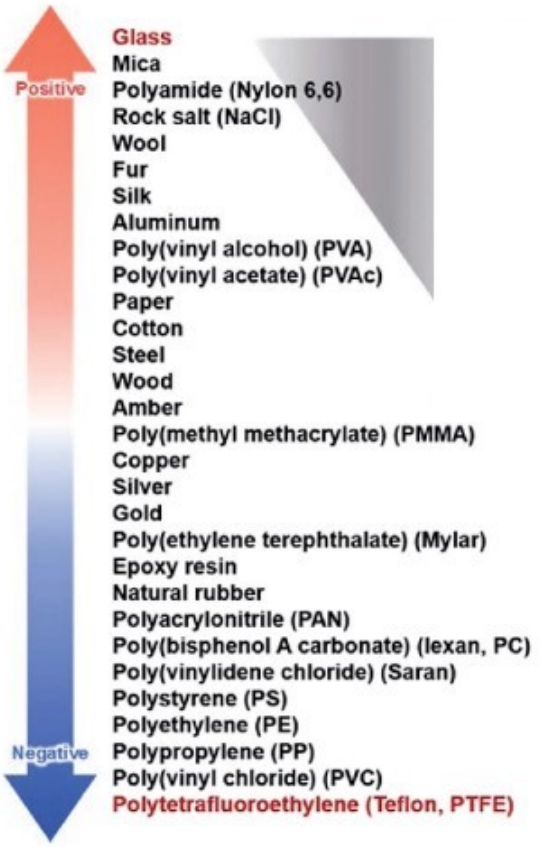

Figure 1.2: The triboelectric series for some materials.

Triboelectricity is typically thought to be caused by the flow of electrons from one substance into another during touch that occurs when two materials come into contact. A well-known series pictured in **Fig.1.2**, known as the triboelectric series, has been widely accepted as a reference. Accordingly, it is as though the two objects are charged, one as the anode and the other as the cathode. The various electronegativities resulting from variations in the molecular and/or material structures are thought to be the primary cause of triboelectric charging. This charge has to remain stable on the surface, indeed Triboelectric materials have limited conductivity or are frequently insulator. Due to the aforementioned discrepancy, there is one side that emits electrons and one that takes them. If this state persists, triboelectric charges are produced on the surface. Consequently, it is possible to develop a list of materials that are more prone to behave as cathode(+) or anodic(-), as illustrated in **Fig.1.2**. This mechanical energy, inducing electrostatic charges, can be converted into electrical energy, thus, using a generator. The most

known triboelectric generator is Van de Graaff generator, it dates back to 1929. It makes use of the static charges that have accumulated due to triboelectrification. A straightforward Van de Graaff generator consists of two rollers of various materials, one of which is encircled by a hollow metal sphere, and a belt made of rubber (or another flexible dielectric material), as illustrated in **Fig.1.3** Van de Graaff

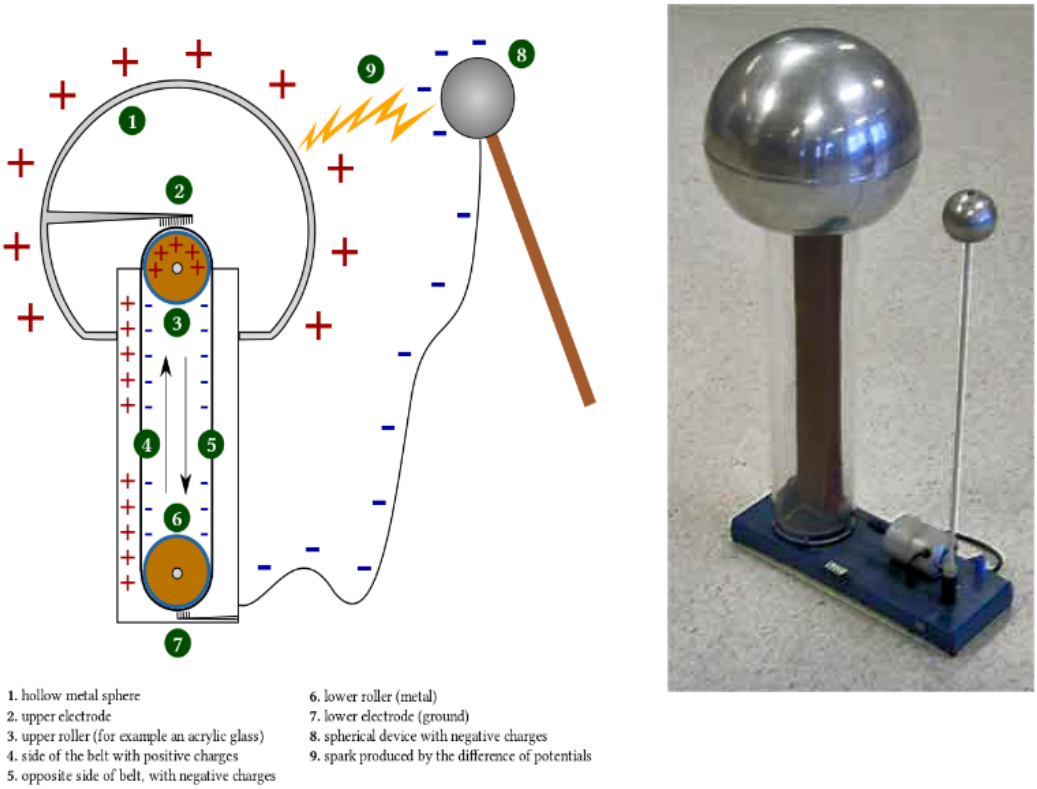

Figure 1.3: Van de Graaf generator. [3]

generators are high voltage sources; without discharge, there is no current. An predicted maximum voltage for a polished, spherical electrode with a diameter of 30 cm is 450 kV. In this project a nanogenerator is examined, so lower values of voltage are involved, indeed it is applied to energy harvesting.

1.2 Energy harvesting

Generally speaking, energy usually denotes the power needed to run a factory, a city, or a country. This is generally referred to as mega energy, which is

quantified on the order of gigawatt or megawatt. The overall power production, stability, conversion efficiency, and cost are the general features of macroscale energy technology. Cost is often the most crucial factor to consider. The increasing requirement for energy is one of this generation's biggest technological obstacles. Humans use an average of 1-2 % more energy per year, and most of that energy comes from fossil fuels [4]. In order to accommodate this increase while reducing climate change, energy consumption, and alternative energy sources are becoming to emerge. Moreover, with the tremendous increase in the number of portable electronics, developing energy harvesting technologies is essential because most of which are run by batteries.

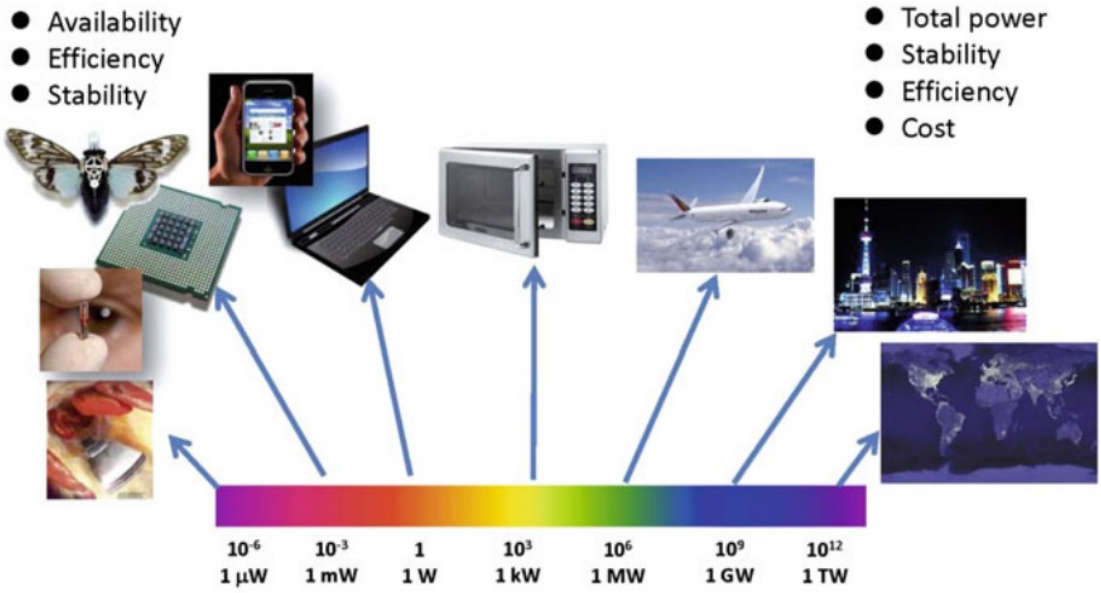

Figure 1.4: Magnitude of power and its corresponding applications, from [5]

Although the power consumption of each device is quite small, the total number of them is extremely large. With the increase of interconnection and automatisation around the globe, a gigantic number of sensors will be distributed worldwide, powering such a wide network of sensors would be time-consuming and expensive for maintenance using only batteries, because one has to find the location, replace them, and inspect the proper operation of batteries from time to time. Harvesting the energy from the environment in which the senor is employed is a possible solution. This is the field of miniaturised energy, which is the power for sustainable, maintenance-free and self-powered operation of micro/nanosystems, whereas macroscale energy is to supply a city and even a country as in **Fig.1.4**. To improve

the efficiency, stability, and dependability of nanogenerators, more research is required. For each application, the best electrical and structural designs and material choices may be predicted using optimization methods for designing nano-generators. The output power density and service life of this improved nanogenerator design can be increased. For example, to increase nanogenerators' endurance to wear, high temperatures, and humidity variations, effective packaging solutions are required. Improved packaging and the use of durable materials can increase the reliability of nanogenerators [6]. Harvesters may not be able to replace any of the major energy sources such as fossil fuels or nuclear power but can decrease the need for these in some situations. Until now, almost all the sensors have been supplied by electric current taken directly by power grids or batteries, which represent not only an additional weight but also a waste difficult to dispose of.

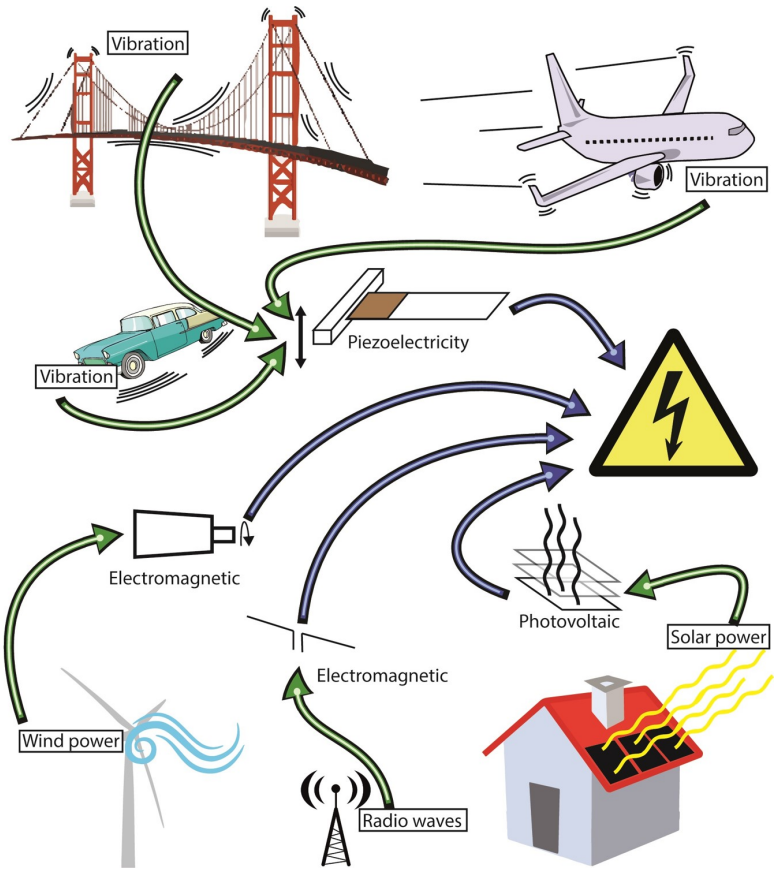

Figure 1.5: An illustration of many potential environmental energy sources that can be used to power intelligent wireless sensor systems.

Moreover, batteries have limited life and need to be replaced, so it is necessary

to place them in easily accessible positions. However, this is not always possible, especially when talking of automotive applications, for example. It appears clear that batteries have a lot of issues that would be better to overcome. Another important trouble of a massive usage of electronics is that the majority of energy consumed today comes from natural non-renewable resources. Many researchers are focused on looking at alternative ways to overcome a possible energy crisis. An interesting solution can be represented by energy harvesting characterised by clean and self-sufficient power sources. The expression ”energy harvesting” refers to the capability of electronic devices to scavenge energy directly from wasted energy present in the environment where they are situated. Thanks to energy harvesting devices it is possible to recover a lot of energy that otherwise would be wasted as in **Fig.1.6**. The range of application is exceptionally broad, for instance, at the same time, it is possible to keep track of the health of buildings and machines and harvest energy from the presence of an electromagnetic field, radio waves, and heat vibrations. If they are correctly managed and monitored, they will consume less energy resources and produce less pollution.
In particular mechanical energy harvesting is the subject of this project. In fact, there are a lot of sources of kinetic energy such as vibrations, wind, water wave, human motions, and vehicle motions that cannot be efficiently harvested using a conventional approach because otherwise are wasted. This is due to the fact that these sources are characterized by very low frequencies and so it is necessary a new technology to store the energy produced by them. This energy can produce the power supply needed to feed the sensor; therefore, an external power supply or a battery is not needed, and the quantity and length of cables are reduced, in this case they are called "self-powered sensors". Measurements are more accurate

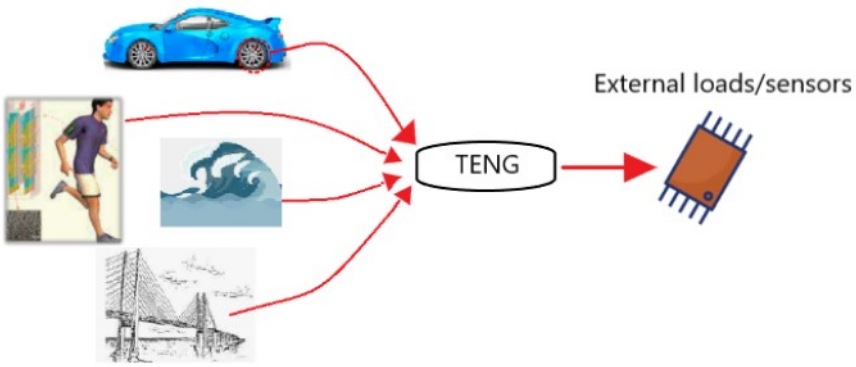

Figure 1.6: Visualization of mechanical energy harvesting from different sources.

when there are numerous wireless sensors connected to a network through WiFi or Bluetooth, since they may exchange data with one another[7].

1.3 TENGs working mode

One crucial aspect in the development of a TENG is the correct exploitation of triboelectrification. To enable triboelectrification that can be adapted to a particular TENG structure, the appropriate mode of operation must be developed to ensure effective use of the external mechanical energy source of the environment. There are four working modes, which are depicted in **Fig.1.7**: the contact-separation (or vertical contact) mode, the linear sliding mode, and the freestanding mode. The vertical contact mode is based on the contact separation process of two various

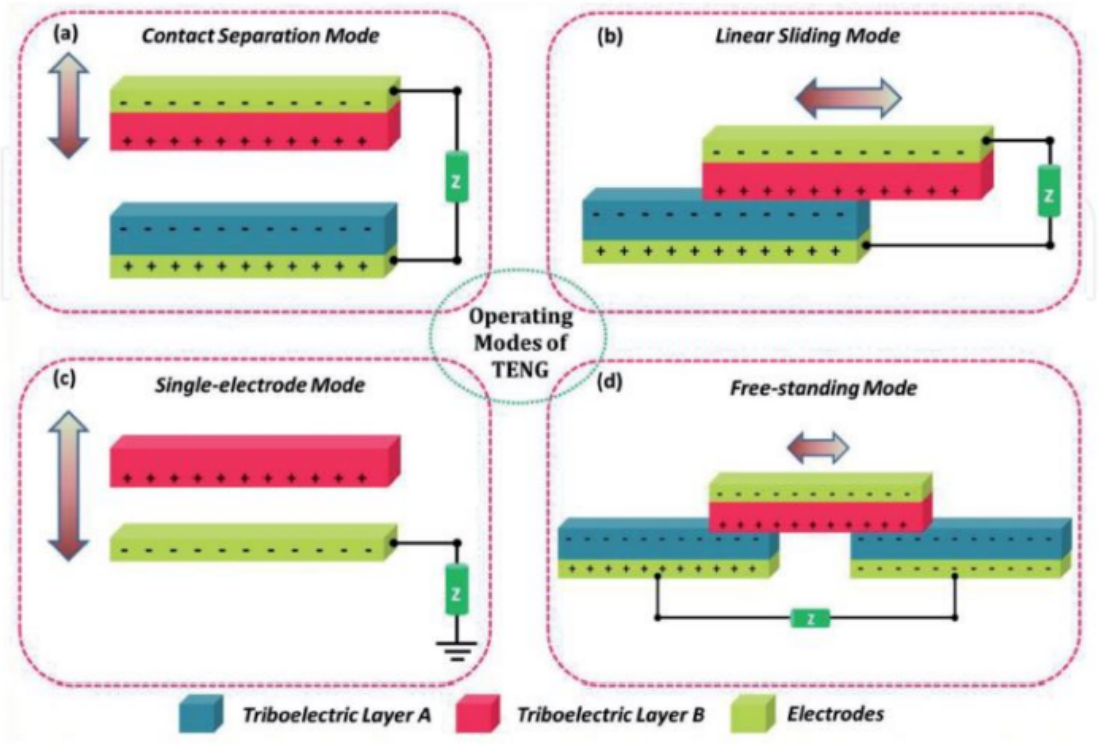

Figure 1.7: The four working modes of TENGs [8]

triboelectric materials, as suggested by the name. When they first come into contact, the two layers are separate and neutral; nevertheless, because the two materials are joined, the entire system remains neutral despite the more triboelectrically positive

left electrons favoring the more triboelectrically negative ones [8]. The device's two pieces display an equal and opposing surface charge when they are separated once more. Equivalent and opposite charges manifest in the corresponding electrode in order to preserve the electric balance, and as a result, there is a voltage difference between the electrodes. This same process can happen also between the dielectric and the electrode, as it is in the configuration examined during this thesis project. In correspondence with the greatest displacement, the maximum voltage difference is obtained.

In the linear sliding mode, a relative sliding in parallel of the two components produces charges on the surfaces. It is worth pointing out that sliding can also be a cylinder or disc rotation in addition to a planar motion.

In the previous two cases, both the dielectrics were connected to an electrode, whereas in the single electrode mode one dielectric is free and only the other one is attached to an electrode [8].

The free-standing mode uses a single, freely movable sheet of triboelectric material to charge two distinct pieces of triboelectric material that are each attached to two electrodes. Due to the close proximity of these final components and the tendency of charges of the same species to reject one another, each piece develops an asymmetric charge distribution as it polarizes [8]. Each of these configurations can produce very different outputs and are one can be more can fit better some applications than others.

1.4 Working principle

The operation principle of a TENG with vertical contact separation mode can be described by coupling contact electrification and electrostatic induction. At original state, the two layers are not in contact, and no charge is produced, with no electric potential difference between the two electrodes. through an externally imposed displacement, the kapton and the electrode comes into contact with each other. The triboelectric effect then causes surface charge transfer to occur in the contact area. It is important to note that the insulating property of the polymer enables the long-term preservation of triboelectric charges for hours or even days [9]. Charges with opposite signs coincide at nearly the same plane since they are restricted to the surface, effectively producing no electric potential difference between the two electrodes. After the separation of the two polymers, a potential difference is created between the two electrodes in an open circuit since the opposite charges are no longer in contact. **Fig.1.8** depicts the fundamental layout of the contact-

separation TENG. There are two dielectric films with their relative permittivity

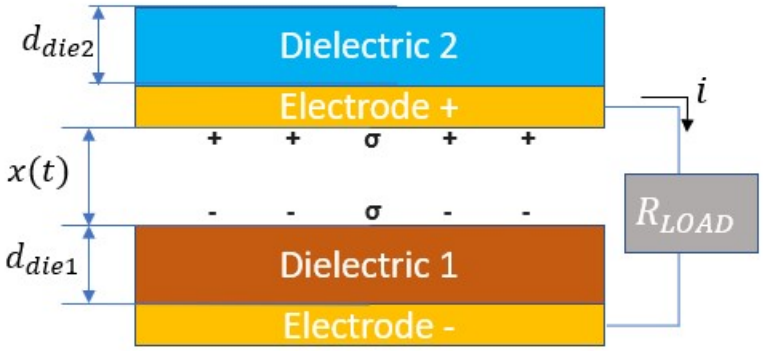

Figure 1.8: Sketch of the TENG circuit

(ε_1, ε_2) and thickness (d_1,d_2), each of them is stacked to one copper electrode. The choice of dielectric materials is important because any material is characterised by a different surface charge density σ, some example of the polymer mainly used as dielectric films for the TENGs fabbrication is in **Fig.1.9**.

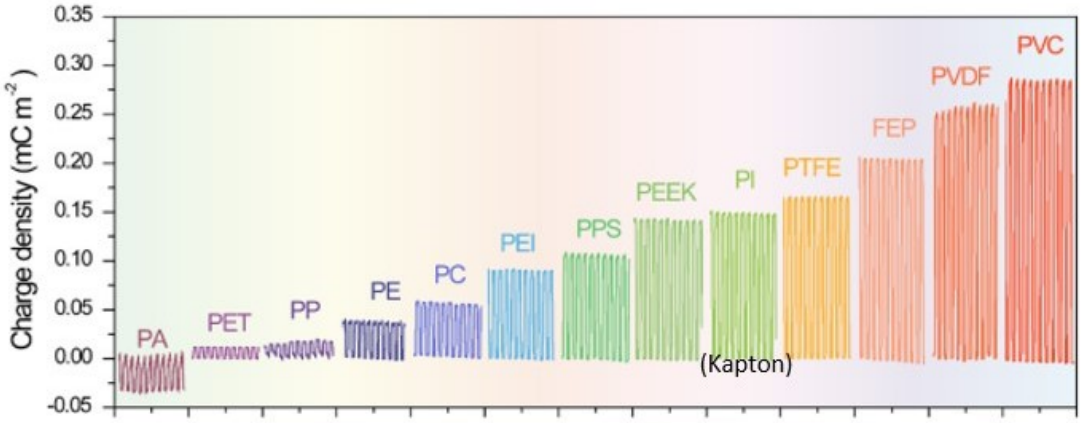

Figure 1.9: List of polymers with their triboelectric surface charge density [10]

The higher the charge difference between the two dielectrics, the better the final performance of the nanogenearator. Here, the charge density with regard to a number of different polymers is measured to quantitatively standardise their triboelectric series with respect to a liquid metal (e.g. mercury), which is easily shape adaptable and elastic to offer the best surface interaction with the substance. It is possible to obtain accurate values by contacting and separating the liquid

metal while maintaining the same contact pressure and considerably increasing the contact closeness, in a glovebox under controlled circumstances, using constant pressure, humidity, and temperature, as in [11].

According to the sketch in **Fig.1.8** it can be modelled as a sereies of 2 capacitance. One is constant due to the thickness of the dielectric 1 d_{die1}, while the second capacitance is variable depending on the gap x.

$$\frac{1}{C} = \frac{1}{C(x)} + \frac{1}{C_{die1}} \tag{1.1}$$

$$C = \frac{C(x) \cdot C_{die1}}{C(x) + C_{die1}} = \frac{S \cdot \varepsilon_0}{\frac{d_{die}}{\varepsilon_{r,die1}} + x(t)} \tag{1.2}$$

In this way, applying a sinusoidal displacement $x(t)$, the equivalent capacitance is "the inverse" of a sinusoidal, it is not infinite for $x = 0$ though because of the constant capacitance due to the presence of the dielectric, it is in phase opposition with respect of the displacement. To make this computation (**Fig.1.10**) the data from the same Kapton of the experiments have been used.

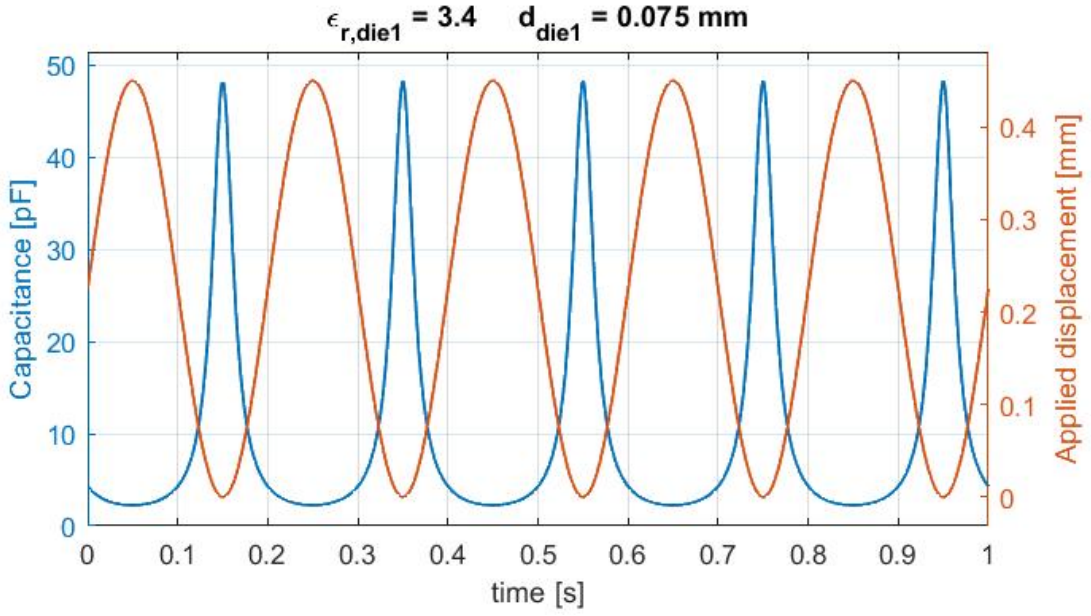

Figure 1.10: Capacitance obtained from a sinusoidal displacement

For what concerns the voltage we have to use the Kirchhoff and Gauss' laws.

$$V = E_1 \cdot d_{die1} + E_{gap} \cdot x(t) = -\frac{Q}{S\varepsilon_0} \cdot \left(\frac{d_{die1}}{\varepsilon_{r,die1}} + x(t) \right) + \frac{\sigma x(t)}{\varepsilon_0} \tag{1.3}$$

Where in **Eq.1.3** the last term stands for the open circuit voltage V_{OC}, it depends only on the surface charge density of the dielectric 1, and on the applied displacement, if x(t) is linear, the V_{OC} will be linear as well. However if x becomes to large, the assumption of a capacitance with infinitely large plates is no longer applicable and edge effects will appear, in this case the open-circuit voltage will diverge from the linear relationship in this circumstance.

Then adding a resistive load to the circuit, it is possible to retrieve the charge transferred in time using the 1^{st} Ohm's law and the voltage can be expressed as:

$$V = R \cdot i = R \cdot \frac{dQ}{dt} \tag{1.4}$$

Then matching **Eq.1.4** with **Eq.1.3** we have:

$$R \cdot \frac{dQ}{dt} = -\frac{Q}{S\varepsilon_0} \cdot \left(\frac{d_{die1}}{\varepsilon_{r,die1}} + x(t) \right) + \frac{\sigma x(t)}{\varepsilon_0} \tag{1.5}$$

By establishing the initial condition, it is possible to solve this first-order ordinary differential equation and find the charge vs time. At time t=0, two plates are close to each another, when charge Q is null. Then, the top plate starts to separate from the base plate. This ODE can be solved with a Simulink model in **Fig.1.11**, using the following parameters, applying, as input, a sinusoidal displacement with frequency $f = \frac{v}{x_max}$, as developed in [12]

Dielectric thickness d_{die1}	$75\mu m$
Surface area (S)	$6cm^2$
Surface charge density σ	$8\mu C/m^2$
Relative permittivity of the dielectric $\varepsilon_{r,die1}$	3.4
Maximum displacement x_{max}	$0.45mm$
Velocity of the upper layer v	$0.5m/s$

Table 1.1: Parameters for the Simulink model

With these parameters, a sinusoidal displacement is applied to the upper electrode.

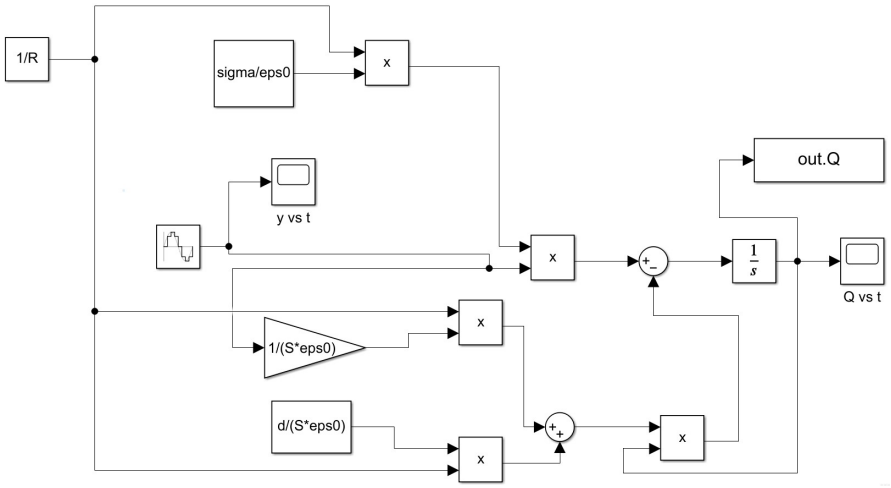

Figure 1.11: Simulink model to solve **Eq.1.5**,(reuse of implementation from [12])

The parameters used to develop this model are reported in **Table 1.1**. The final output is the charge transferred **Fig.1.12**

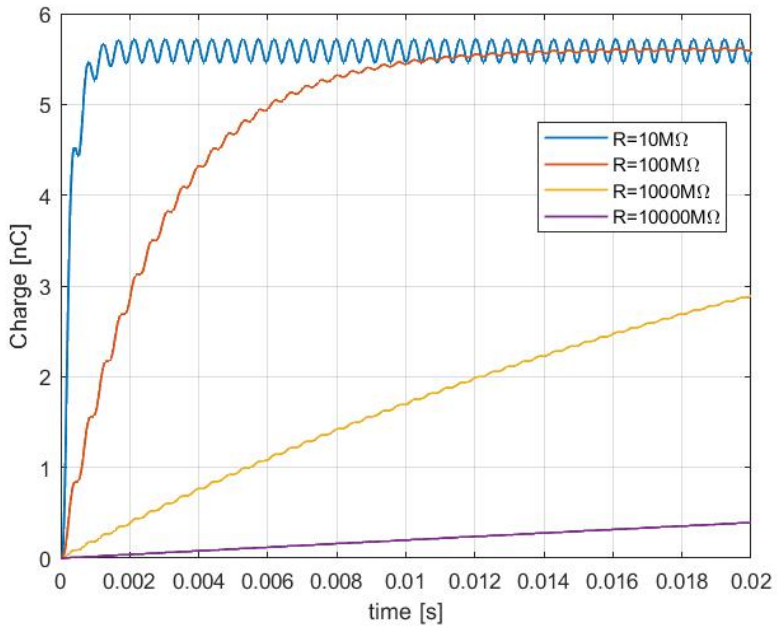

Figure 1.12: Charge variation in time for different values of the resistance connected to the TENG

The lower R, the faster is the rise of charge to a stable mean value. Indeed, a TENG connected to a resistive load can be seen as a simple RC circuit, and it is deducible that the time constant is:

$$\tau = RC \tag{1.6}$$

If resistance goes up, τ will increase and the time to reach the final asymptotic value will grow. When a resistive load R is connected with a TENG the output current and voltage, and consequently power. can change drastically depending on the resistive load value, as happens in **Fig.1.13**. The working of the TENG

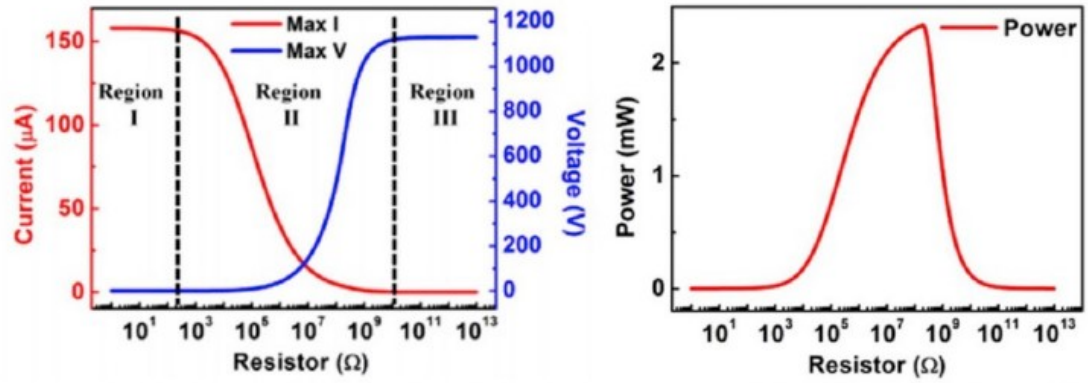

Figure 1.13: The values of the voltage,current and power on different loads of typical TENGs. [13]

could be regarded as three operation regions. Region I, in which resistance is low ($0.1 \div 1000\ \Omega$), the peak value of current has dropped a little from the SC state, while the maximum voltage is nearly proportional to the outer resistor. Region II, the maximum current decreases with the resistance while the voltage behaves in an opposite trend, and the TENG obtains its maximum output power. Region III, when the resistance is larger than 1 $G\Omega$, the maximum voltage saturates at V_{OC}. It is important to know the maximum power obtainable from TENG and for which value of resistance it appears, this analysis will be experimentally characterized in the section section 3.3

Indeed, when it comes to energy storage from TENGs, we have to deal with power management. Triboelectric devices (even for tire applications) are not recommended to drive most electrical devices directly because of the discontinuity, changeable frequency, and irregular amplitude of TENG outputs. To make a deeper

analysis of the behavior of the TENG in a more complex circuit (with more resistors, capcitors, inductors, etc.), this can be modeled in the SPICE software as proposed by [14].

1.5 Implementation in tires

Due to the extremely intensive use of vehicles, the rapid growth of automotive technology in the world leaves room for the production of waste mechanical energy. Many reports say that the population of vehicles would increase rapidly and reach billions in 2030 mainly from countries such as India, China, and the USA [15]. The mechanical energy waste from vehicle motion can be converted into useful electrical energy and has been used to power a few of the automotive electronics systems, such as sensors; this procedure is called tire condition monitoring system (TCMS). Many firms are working on developing smart tires with TCMSs that can track variables such as the coefficient of friction between tires and the road surface, vehicle speed, tire pressure (TPMS), and tire load. Additionally, an energy harvester has a very high acceleration, therefore, if the added mass of the harvester is too high, it can undergo really high centrifugal force. So, the energy harvester should also be lightweight to guarantee rotational equilibrium of the tire.

The idea of implementing energy harvesters into tires first starts with the piezoelectric cantilever beam, but there are some disadvantages such as the too narrow space between the wheel rim and the actual tire, and, second, a beam is easier to break. A valid alternative can be the use of flexible piezoelectric harvesters made of PVDF, a piezoelectric polymer. In this project, the use of triboelectric harvesters has been analysed.TENGs have more advantages such as lower operating frequency, high power density, easy fabrication, and lower cost, indeed, all materials can be recycled as shown in [16] . These advantages gain more attention towards TENG based energy harvesting which is also cheaper than piezoelectric. This makes TENG a suitable energy harvester for tires. The tire undergoes the weight of the car, and a flat area where the tire is in contact with the ground is created as in **Fig.1.14**, this zone is called contact patch area A new area of the tread deforms within the contact patch when the tire spins during vehicle motion, creating a pattern of cyclic deformation and relaxation. To study energy harvesting from the TENG, it is attached inside a rolling tire **Fig.1.14b**, while it goes through the bending zone represented in **Fig.1.14a**, the TENG produces energy thanks to the bending and the change of its capacitance due to the change of the air gap between the two layers. On the other hand, piezoelectrics work better as

sensors. However, as the existence of intrinsic capacitance, TENG has a large

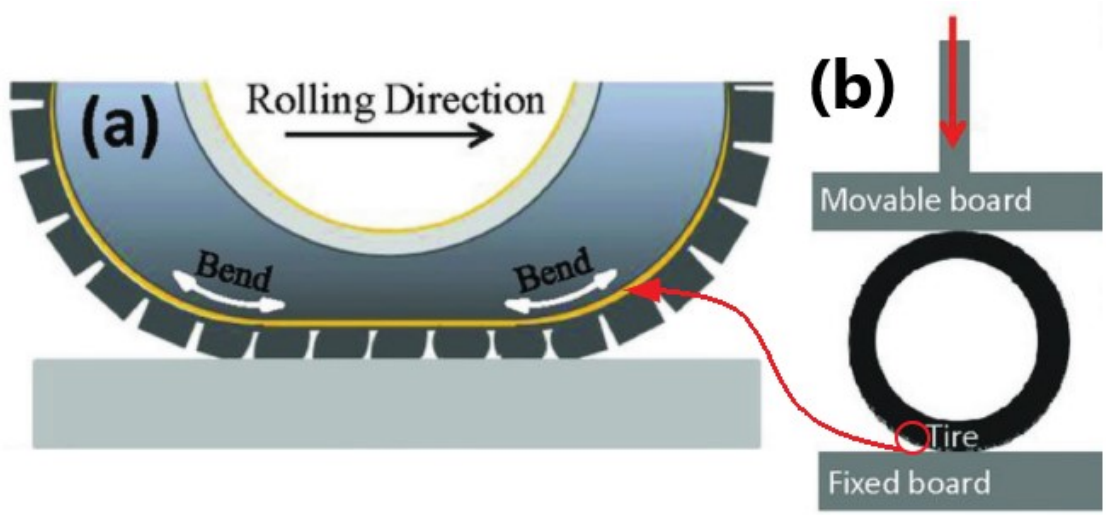

Figure 1.14: a. Shape change of the tire in the contact patch **b.** Sketch for testing the harvester.

internal impedance of typically in several Mega ohms' level [13]. So TENG usually has a large voltage of hundreds of volts and small current in μA level. Since the impedance of electronic device and energy storage unit is relatively low, the energy transfer efficiency would be very low when TENG is directly used as a power source. In addition, the viability of TENG's renewable power output would be reduced without energy storage. For example, when the mechanical energy does not exist or the average power isn't sufficient for the working of commercial electronics, the power supply would become invalid. For sustainable power sources, TENG and energy storage device need to be combined complementarily. Compared with traditional energy source, TENG has the great to be of flexible and stretchable. Consequently, developing a flexible estimation structure to operate the available sensor data in production vehicles is a leading objective of the car manufacturers [17].

Chapter 2

Simulation results

2.1 COMSOL model

COMSOL Multiphysics is a cross-platform finite element analysis, solver, and multiphysics simulation software. It allows conventional physics-based user interfaces and coupled systems of partial differential equations (PDEs). COMSOL provides an IDE (integrated development environment) and unified workflow for electrical, mechanical, fluid, acoustics, and chemical applications. Triboelectric nanogenerators function works by coupled effects of contact electrification and electrostatic induction to convert mechanical energy into electric energy. It is enough considering the electrostatics physics on COMSOL to retrieve the open circuit voltage and the short circuit charge. Later the solid mechanics physics will be added to simulate mechanical pressure applied by the tire deformation on the TENG.

A triboelectric nanogenerator is subject to all the rules of electrostatics that are applicable to electrostatics in general. The electric field of a system may be described by the following equation when the scalar quantity of the electric potential, is taken into consideration. expressed by the following equation:

$$\mathbf{E} = -\nabla V \tag{2.1}$$

Electrostatics follows Gauss's laws, which states that *"the flux of the electric field E generated by a system of charges through a closed surface is proportional to the algebraic sum of the electric charges enclosed by the surface"*[18]. In its integral

form, this law can also be written as follows:

$$\Phi_E = \oint_S \mathbf{E} \cdot \mathbf{u_n}\, dA = \frac{Q}{\varepsilon_0} = \int_V \frac{\rho}{\varepsilon_0}\, dV \tag{2.2}$$

where dA is the infinitesimal area of the surface through which the flux passes, ϕ_E, caused by the electric field E, u_n is the normal vector pointing outward, Q is the electric charge which is inside the hypothetical surface, ε_0 is the vacuum permittivity, ρ is the total electric charge density of the system expressed per unit volume and dV is the volume element enclosed by the hypothetical surface. Guass's law of **Eq.2.2** can be equivalently written in its differential form by means of the divergence theorem:

$$\nabla \cdot \mathbf{E} = \frac{\rho}{\varepsilon_0} \tag{2.3}$$

Regarding dielectric materials, it is then possible to express the electric induction D generated by the electric field acting upon a dielectric

$$\mathbf{D} = \varepsilon_0 \mathbf{E} + \mathbf{P} \tag{2.4}$$

where P is the electric polarisation, a vector field of the density of electric dipole moments in a dielectric material, which in a linear, homogeneous and isotropic dielectric is directly proportional to the electric field itself:

$$\mathbf{P} = \chi \varepsilon_0 \mathbf{E} \tag{2.5}$$

where χ stands for the electric susceptibility of the dielectric material. The polarisation density also describes how a material responds to an applied electric field and the way the material changes the electric field. Therefore, introducing the relative permittivity of the dielectric medium which is function of its electric susceptibility, $\varepsilon_r = 1 + \chi$, and given that the absolute permittivity of the dielectric ε is the product of the relative permittivity times the vacuum permittivity, it is possible to express **Eq.2.4** as follows:

$$\mathbf{D} = \varepsilon \mathbf{P} \tag{2.6}$$

Considering once again the outcomes of Gauss's law of **Eq.2.3** yields:

$$\nabla \cdot \mathbf{D} = \rho_f \tag{2.7}$$

with ρ_f being the number of free charges per unit volume. In **Fig.2.1** it is shown

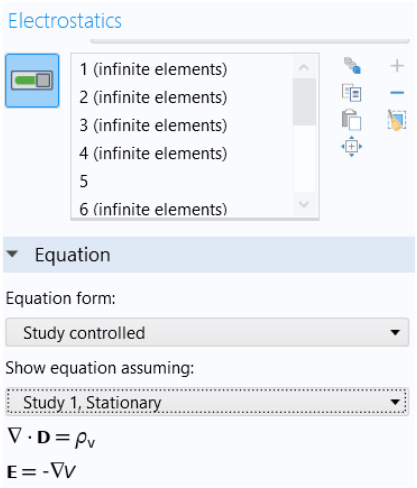

Figure 2.1: Electrostatics module from COMSOL

that **Eq.2.1** and **Eq.2.7** are used in the electrostatics module of COMSOL.

This relations built in COMSOL derive from the more generalised Maxwell's equations in vacuum, reported in the differential form, a set of four equations coupled 2 by 2:

$$\nabla \cdot \mathbf{E} = \frac{\rho}{\varepsilon_0}; \quad \nabla \times \mathbf{E} = -\frac{\partial \mathbf{B}}{\partial t}; \tag{2.8}$$

$$\nabla \cdot \mathbf{B} = 0; \quad \nabla \times \mathbf{B} = \mu_0 \left(\mathbf{J} + \varepsilon_0 \frac{\partial \mathbf{E}}{\partial t} \right); \tag{2.9}$$

Considering only the electric field physics and a stationary study, the terms depenging on time and on magnetic induction are elided. Therefore we come back to the equations used in COMSOL and there is only the first two equations regarding the electric field (the electric charge conservation and the Stokes'law).

2.2 Sliding contact mode

Having selected the physics, the next step is to define the geometry. For the case of the sliding contact mode, we choose the same as in [19] and illustrated in **Fig. 2.2**, it is a 2D geometry in COMSOL, to simplify the calculation (instead of a 3D model). The dimensions of the two dielectrics were 10 cm in the longitudinal direction (l) and 0.22 mm in the thickness direction (represented by d_1 and d_2).

The two dielectric layers were joined together with two metal electrodes that had a thickness of 0.01 mm. While the top could move in the longitudinal direction, the bottom portion was locked. x was used to establish the lateral distance. The triboelectric effect is responsible for the charges having different signs in the non-overlapping parts of the lower surface of Dielectric 1 and the top surface of Dielectric 2. It is acceptable to assume that these triboelectric charges (tribo-charges) are equally distributed on these two surfaces because of the nature of this phenomenon, which is a great approximation for insulators.

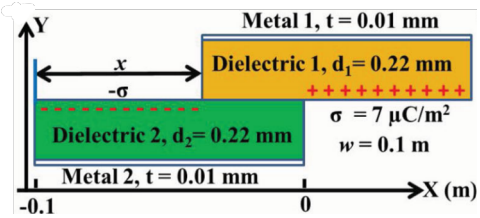

Figure 2.2: Sliding contact geometry. [19]

2.3 Boundary condition

Secondly, the ground will be chosen as the infinite domain's outer border, as going further from the electrodes, the voltage becomes homogeneous. On these insulating polymers, the tribo-charges' natural deterioration over time may be disregarded. Because the distance between the centers of the positive charges and the negative charges is at the atomic level, the total density of tribo-charges on the overlapping surface may be taken to be 0. The tribo-charges' surface densities are σ $(7\mu C \cdot m^{-2})$ at the surface of the dielectric 1 and ($-\sigma$) at the surface of the dielectric 2 as in [19]. Because it is typical in experiments, air surrounds the whole device. The reference point for electric potential, which is zero, is the potential at infinity. Then, to define the open circuit condition, the floating potential boundary condition is assigned to the electrodes, and now the model is ready to be meshed. To apply the SC boundary condition, the two electrodes were assigned the same electric potential. In addition, to maintain charge equilibrium, the summation of the charges at the two electrodes was assigned as 0. As study, has been chosen a stationary one, as the position of the top layer is going to change, moving from the original position to the right-hand side, a parameter sweep is useful. This relations built in COMSOL derive from the more generic Maxwell's equations, a set of four equations coupled 2 by 2:

2.4 Results

A relative sliding parallel to the surface produces triboelectric charges on the two surfaces of two dielectric films when they are in touch. In order to entirely balance the field produced by the triboelectric charges, a lateral polarisation is thus supplied along the sliding direction. This causes the electrons on the top and bottom electrodes to flow. The electric potential of the top electrode is positive while that of the bottom electrode is negative due to the electrostatic induction of the tribo-charges. In **Fig.2.3** is the electric potential in the 2D domain of the element model from COMSOL, it can be noticed that, as the upper dielectric moves rightward, the difference in the voltage increases and becomes more symmetric. Regarding the open circuit voltage, with the increase of x , the open-circuit electric

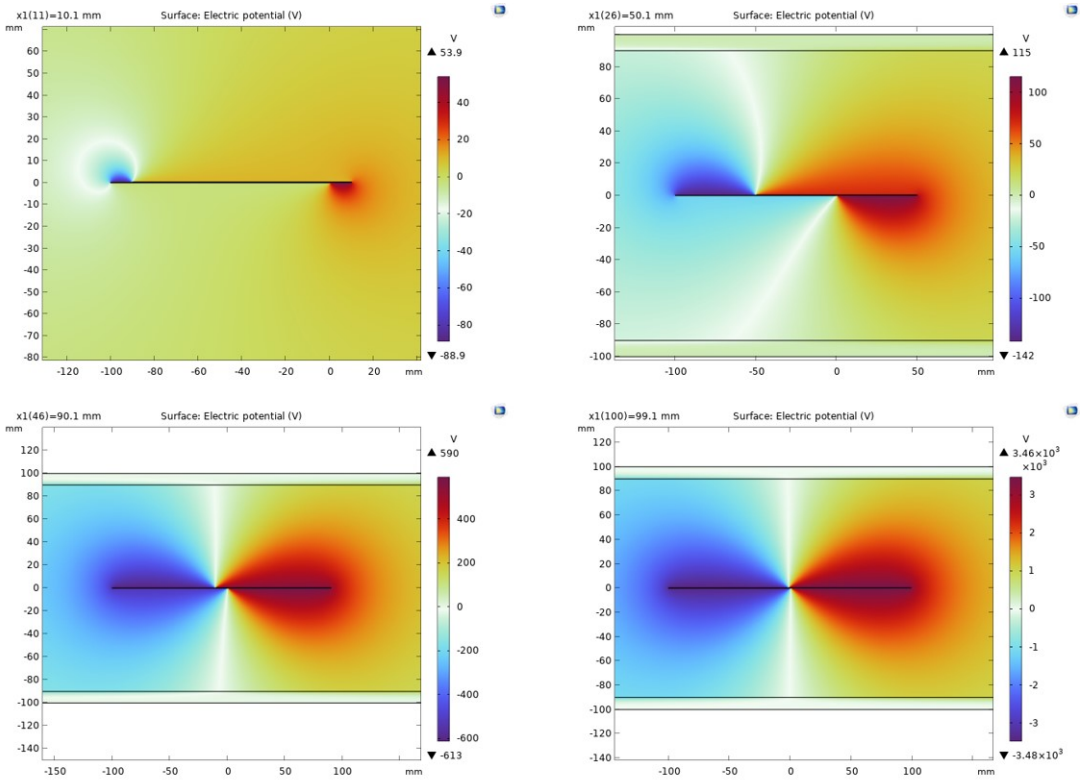

Figure 2.3: Sliding contact electric potential

potential difference (V_{OC}) between these two electrodes also increases. Furthermore, the slope of the $V_{OC} - x$ curve is much higher when x is approaching l as happens in **Fig2.4**. Through the integration of the charges on the bottom electrode, the total amount of transferred charge at SC condition (Q_{SC}) is calculated and its

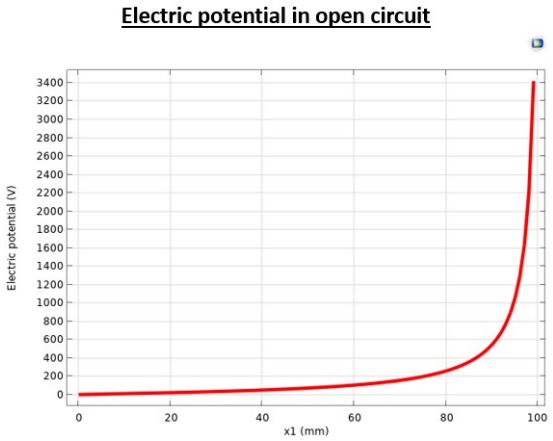

Figure 2.4: Calculated V_{OC} at different x ,

relationship with x is reported in **Fig.2.5**. According to the FEM calculation

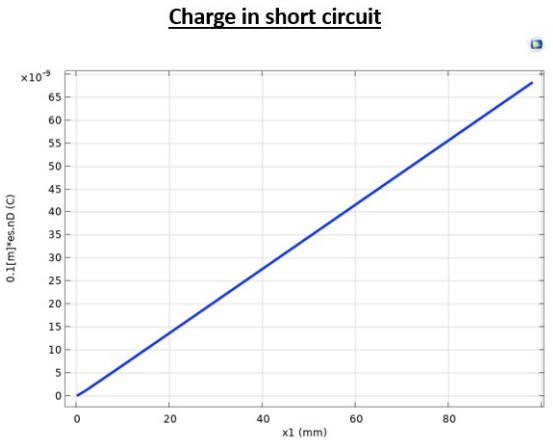

Figure 2.5: Calculated Q_{SC} at different x ,

above, there is a direct correlation between the total quantity of charges that are transported between electrodes and the separation distance x and the voltage output of TENG. Calculating the voltage output of the TENG at various Q and x values allows for the analysis of this relationship, as done in [19] using the following equation .

$$V = -A(x) \cdot Q + B(x) \tag{2.10}$$

Physically speaking, the parameter A represents the reciprocal of the capacitance C created between the two electrodes, while the parameter B represents the voltage produced when Q is equal to 0, or the open-circuit voltage. (V_{OC}). Therefore,

eq.2.10 can be rewritten as:

$$V = -\frac{1}{C(x)} \cdot Q + V_{OC}(x) \tag{2.11}$$

The short-circuit charge Q_{SC} has a linear relationship with x and is obtained to its maximum when x reaches x_{max} . The driving force of this charge transfer is the electrostatic force from the tribocharges. This driving force will provide an "expected" charge transfer rate from the bottom electrode to the top electrode. In case a resistive load is applied, utilizing Kirchhoff's law, the governing equation can be determined by:

$$R \cdot \frac{dQ}{dt} = \frac{1}{C(x)} \cdot Q + V_{OC}(x) \tag{2.12}$$

In conclusion, this chapter presents a theoretical model for the sliding-mode TENG. The distributions of electric potential, electric field, and charges on the metal electrodes of the TENG have been described using the finite element approach. However, in practice, the vertical contact mode is more used because it allows wider applications and has higher output for the same dimensions and materials.

2.5 Vertical contact mode

A first design of the contact-separation mode TENG is illustrated in **Fig.2.6** as explained by [9] Between two polymer layers, a cavity is formed, which is sustained by a spacer and for the charge generation and separation processes.The bottom electrode for the manufacturing was a square glass sheet that had a thin coating of aluminum put on it using an electron beam evaporator. A thin layer of polymethylmethacrylate (PMMA) was then spin-coated followed by the addition of a spacer layer at the centre. The spacer kept the Kapton film at a certain distance from the PMMA layer below and was constituted of an insulating polymer with double-sided adhesive. When triggered by a vibration source with controlled frequency and amplitude, the generator produced an open-circuit voltage and a short-circuit current. Therefore, electrons are pumped back and forth between the two electrodes as a consequence of contact electrification and electrostatic induction.
In order to have an elevated output, the accurate choice of many parameters is

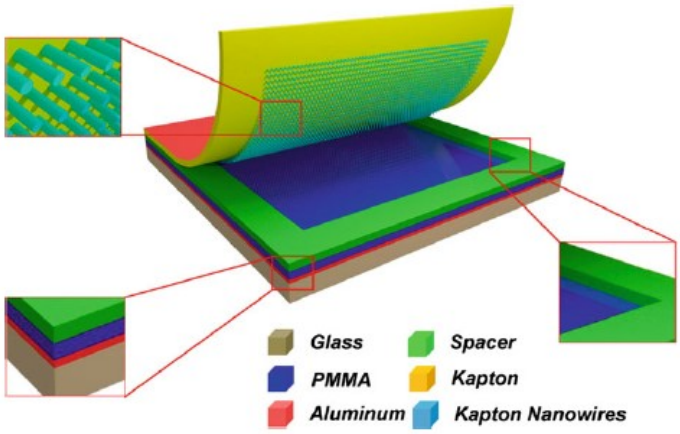

Figure 2.6: Sketch of the generator's structure and materials selection. [9]

important. The first is the appropriate selection of materials. According to the triboelectric series, there is a significant polarity difference between Kapton and PMMA, which causes a very efficient charge transfer upon contact. In addition, the spacer (poly-propilene) structure plays an important role. The spacer's height not only relates to V_{OC} but also affects I_{SC}. Only a very small amount of electrical output could be observed without the spacer. This, together with the conductive tape has to provide a proper restoring spring back, meaning that after the two layers went completely in contact, they must detach and come back to the original position.
Moreover on both sides of the spacer there is a double-sided tape to keep the contact with the other dielectric layers. This tape is also slightly elastic to take back the original width after every tapping. The dimensions are $25mm$ x $60mm$, which are the maximum in order to be have the harvester used in the tire.

2.6 Results

For what concerns the electrostatic, the same boundary conditions of the sliding mode have been applied on COMSOL as depicted in **Fig.2.7**. That is, a 2D model with a surrounding domain of air. As shown in **Fig.2.8**, there is a dipole behaviour in which we have a positive and a negative electrode. The potential changes depending on the distance between the electrodes. From this same simulation, it

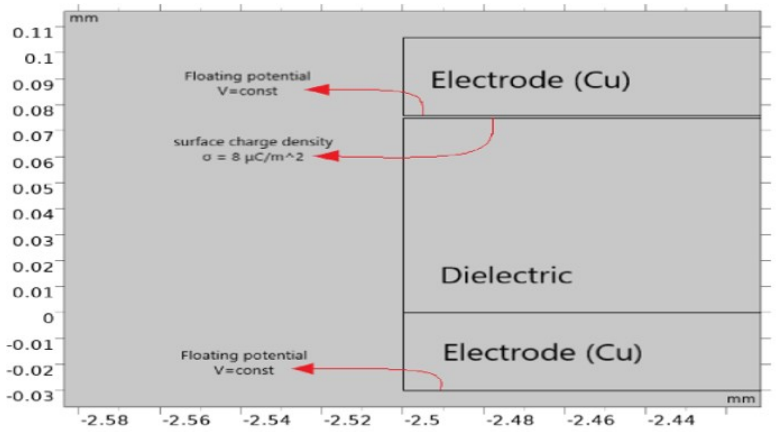

Figure 2.7: Boundary conditions for the electrostatic COMSOL model.

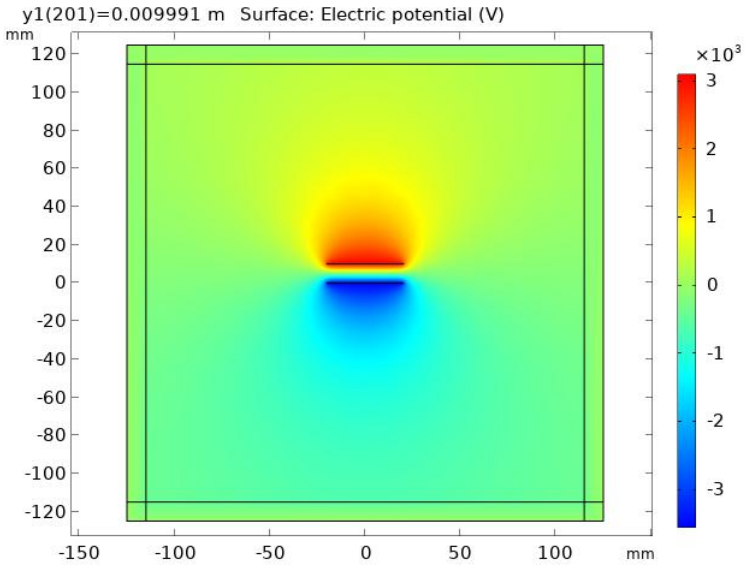

Figure 2.8: Electric potential in the 2D domain

is possible to retrieve electric field displacement in **Fig.2.9**, which represents the free charge density in the dielectric.

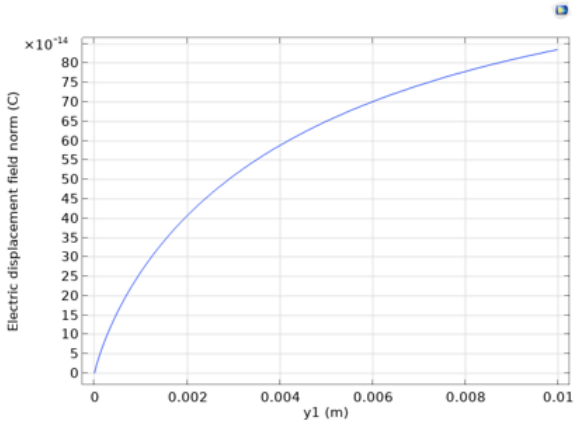

Figure 2.9: Electric displacement field from the electrostatic COMSOL simulation

Two approaches have been used to model the mechanics behaviour:

- 3D model in **Fig.2.10** with shell layers for the triboelectric materials, with a stationary study and a parametric sweep on the load from 0 to 5 MPa applied on the upper surface of the block
- 2D model in **Fig.2.11**. Applying a load of 5 MPa moving at constant velocity of 10 m/s

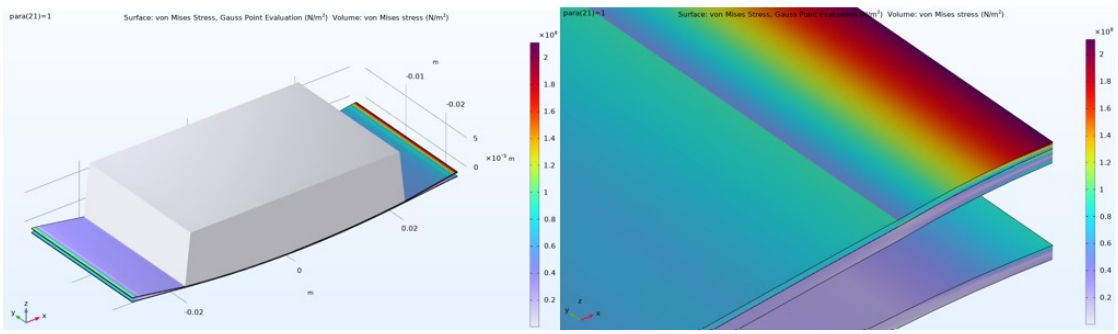

Figure 2.10: 3D stress with a load of 5 MPa on the upper face of the block

It is worth defining that shell elements are a mathematical simplification of solids of special shape. Thin shells (like thin beams) do not consider the stress in the direction perpendicular to the shell surface. In Finite Element Analysis [FEA] shell

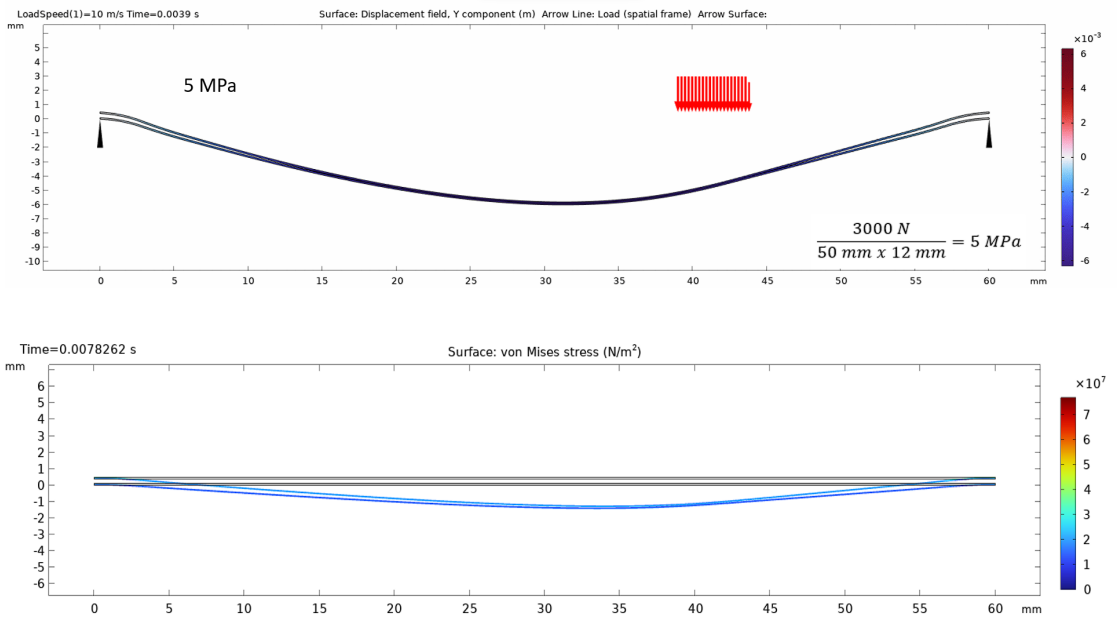

Figure 2.11: 2D geometry and moving load of 5 MPa.

elements can be utilized for effective results. It can lead to huge computational time savings since they allow modelling of thin features with fewer mesh elements. Shell elements are also easier to mesh and less prone to negative jacobian errors which might occur when using extremely thin solid features.
In both simulations, there is the maximum stress at the ends, where the harvester is clamped, and also the maximum value of Von Mises stress is of the same order of magnitude ($\sim$ 100 MPa). Besides, with regard to displacement, it is maximum 6 mm, at Nokian tests it was seen that it was 2 mm. Considering that in the COMSOL simulation there is not the rubber surface to constrain the bottom layer of the harvester, the simulation result can be considered acceptable. As final step of the COMSOL simulation the elctrostatic and solid mechanics physics have been joined, applying the same moving load at 30 km/h and boundary condition same as **Fig.2.11** and electrostatic boundary conditions in **Fig.2.7**.

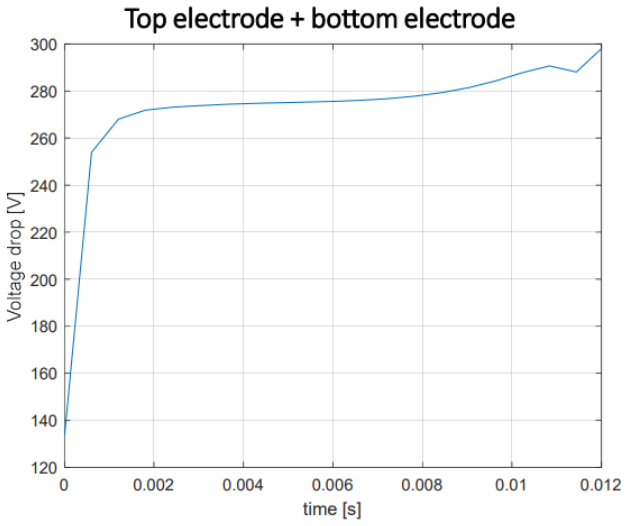

Figure 2.12: Open circuit voltage drop in time

In **Fig.2.12** is depicted the result for only one time in which the load moves from left to right. The voltage increases fast up to a constant value, this means that the two layers are almost completely in contact and the distance between the two copper electrodes is constant as well as the capacitance.

Chapter 3

RISE experiments

3.1 Experimentl setup

The experiments conducted at RISE [20] are presented in this chapter. The triboelectric samples were build according to the **Fig.2.6**. All the samples have in common the Kapton layer on one side. Kapton is a polyimide film used in flexible printed circuits (flexible electronics) and space blankets that are used on spacecraft, satellites, and various space instruments. Invented by the DuPont Corporation in the 1960s, Kapton remains stable (in isolation) across a wide range of temperatures, from 4 to $673K$ (-269 to $+400°C$) [21]. This insulating film has a special set of qualities that make it perfect for a wide range of uses in several industries, for istance electronics manufacturing, spacecrafts and 3D printing. The kapton layer taken in exam in these experiments is $75\mu m$ thick.
The other dielectric layer can be made of PET, FEP (commonly called teflon), or mica. PET (polyethylene terephthalate) is a transparent film material that has reflective properties and high tensile strength. It provides excellent insulation as it forms a barrier against moisture, oil, and grease. It's also resistant to water, varnishes and solvents, making it a good choice for harsh industrial environments. The film can withstand high-impact applications, as it is tear and puncture resistant. The PET layer taken in exam in these experiments is $50\mu m$ thick. Lastly, mica is a naturally-forming silicate mineral, it can be laminated for providing outstanding electrical insulation at high temperatures. It is environmentally safe and nontoxic.The mica layer taken in exam in these experiments is $200\mu m$ thick. There is also a poly-propilene layer (spacer) with a thickness of $450\mu m$.
Before presenting the obtained experimental results, it is useful to understand the conditions in which the tests have been performed. Thus, the following description

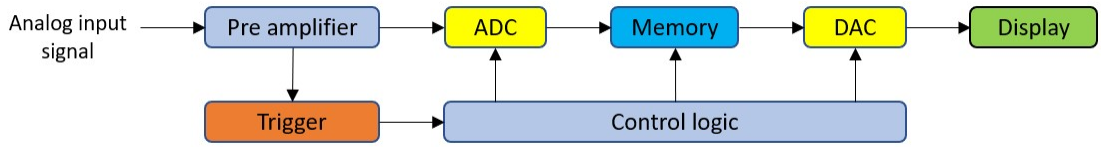

Figure 3.1: Oscilloscope working flow.

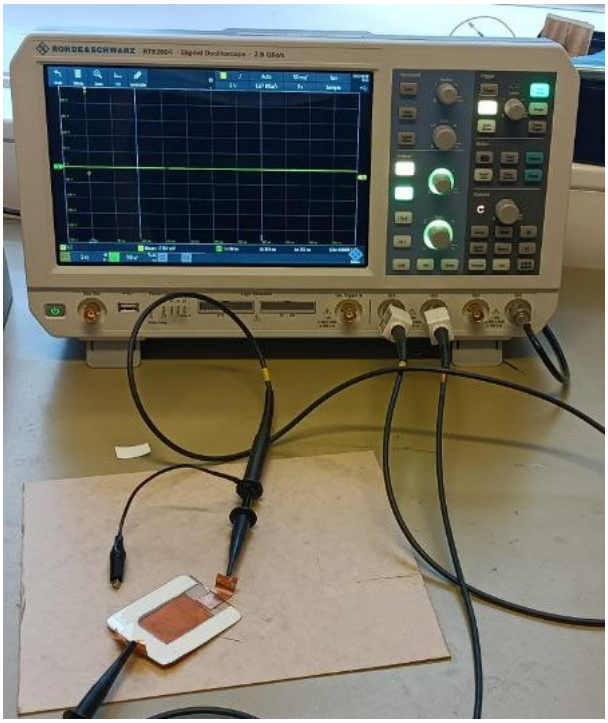

Figure 3.2: Picture during measurements at RISE

has a double purpose: to inform the reader about the working mode and to give the possibility to repeat the tests in order to obtain similar reported results. In order to detect the voltage signal generated by the TENG, a digital oscilloscope (Rhode&Schwartz rtb2004), whose scheme is depicted in **Fig.3.1** and in **Fig.3.2**.

A particular kind of electronic test tool uses a two-dimensional plot of one or more signals as a function of time to graphically represent changing electrical voltages. The sole duty of the trigger system is to instruct the other components of the oscilloscope on which data to pay attention [22]. Since it controls when the acquisition system starts to acquire, it automatically controls what is shown on the screen and what data is accessible for measurements. An analogue-to-digital converter (ADC) transforms the measured voltages into digital data in the case of

digital oscilloscopes. The Nyquist limit of a conventional DSO (Digital Storage Oscilloscope) prevents it from recording signals with a bandwidth greater than half that of the ADC.

3.2 Output without any impedance

In the following picture it is depicted the open circuit voltage between the two electrodes. Firstly it has been analyzed a device with the spacer, and kapton, PET, FEP, mica (only in this case without the spacer) as dielectric layers,always having as reference the **Fig.2.6**, has been taken in exam as dielectric materials kapton, PET, FEP, mica. The TENG has been excited by one impulsive tap, clearly,

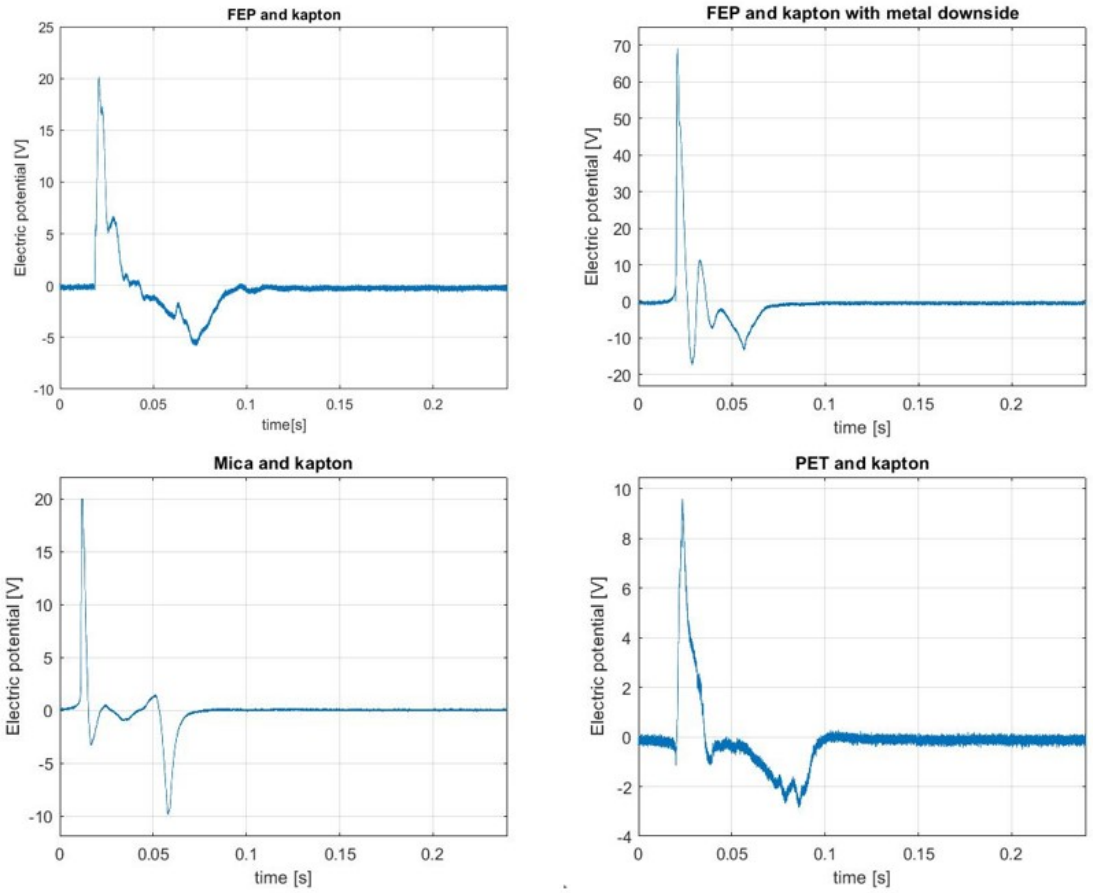

Figure 3.3: Output voltage with the chosen dielectric materials

the voltage (**Fig.3.3**)has the same trend, as expected, regardless of the material;

nevertheless, the amplitude changes clearly. The positive peak correspond to the instant when the two layers come in contact, while the negative peak is when they detaches

The output voltage is almost doubled with teflon instead of PET, since teflon has really high electronegativity, indeed, it has fluorum, the most electronegative element. These results are useful for understanding the output of the TENG depends on its material, shape and dimension, although in order to have a more precise characterisation of the device, it is necessary to always apply the same excitation force; this can be done by means of an instrumented PCB hammer, in **Fig.3.4** , connected to the oscilloscope in order to visualise the impulsive force applied.

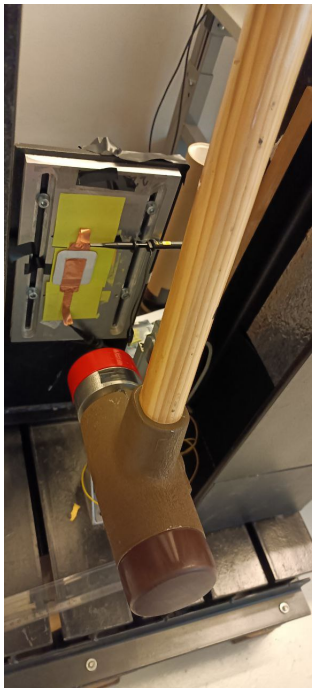

Figure 3.4: instrumented PCB hammer (Model : 086D50)

Another experiment done at RISE was to simulate the bending of the harvester happening in the tire by meaning of a 3d printed channel and force sensor MARK10 from [23] in **Fig.3.5.a**. Through this software can be imposed a vertical displacement to the harvester, which passes through the channel and bends. One drawback of this toll is that the maximum applicable velocity is 1100 mm/min. For this reason the voltage and current assume very low values. Nevertheless it is noticeable a periodic curve **Fig.3.5.b**. Furthermore, increasing the velocity, the

voltage and the current will increas as well as the frequency of the signal.

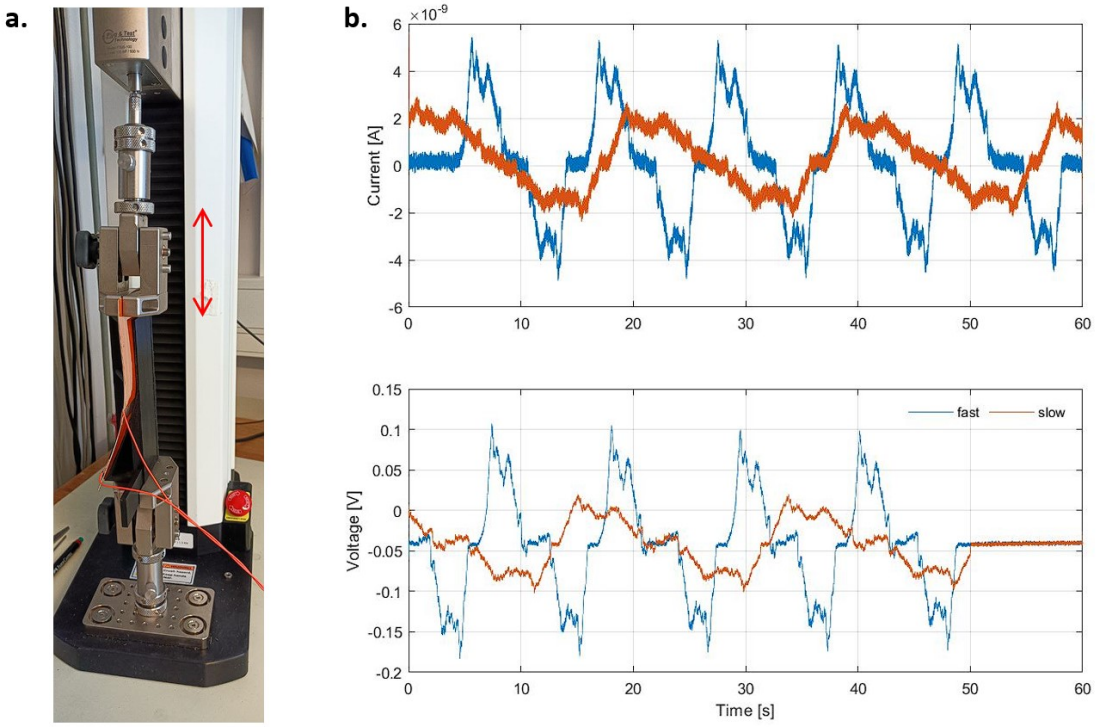

Figure 3.5: **a.**RISE MARK10 for bending **b.**Current and voltage at 1100 mm/min (fast) and 500 mm/min (slow)

3.3 Characterisation of the harvesters

To get the maximum power possible from the harvester, we should connect to it the resistive load at which there is the highest power, in this way the internal resistance of the device can be quantified. To have the power, are measured the voltage at the harvester and by means of the oscilloscope in parallel with the resistive load and the TENG, and the current by means of a current amplifier (Keithley 428) connected in series with the TENG.

The identical current is present everywhere with a series connection, regardless of where you measure. This can be compared to a water pipe: if water enters the pipe at one end, it must also exit the other end in the identical amount. Additionally, the water flows uniformly throughout the pipe. In the series circuit, the electrical voltage is not uniformly distributed. A voltage drop occurs at the

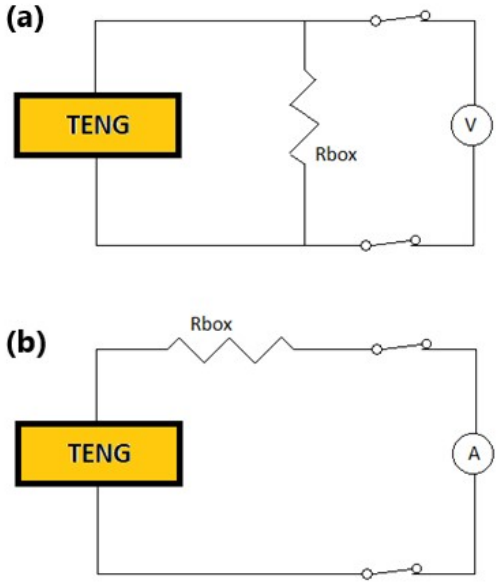

Figure 3.6: Circuits for **(a)** voltage and **(b)** current measurement

first component, where a portion of the voltage is lost, and another voltage drop occurs at the second one. Less voltage is available for the last component when you connect more components in series. In contrast, all components in a parallel circuit experience the same voltage drop. The components are positioned next to one another rather than immediately behind one another, which explains why. However, this also implies that the current throughout the entire circuit is not constant. Again, the water pipe analogy is useful in this situation. If the water pipe divides into two smaller pipes, only a part of the original total current flows through each pipe. For the explained reasons the voltage must be measured in parallel (**Fig.3.6a**) and the current in series connection (**Fig.3.6b**). The resistance was changed through the box in **Fig.3.7**,it contains many resistors of different values, and adding them it is possible to have the desired value of resistance.

During these experiments, the three harvesters reported in **Fig.3.6** have been tested mainly. The metallized PET dielectric is made of a layer of PET that is coated with a very thin layer of indium tin oxide; due to this, in this harvester we do not need a second copper electrode. The overview of the thickness of this geometry can be seen in **Table 3.1**.

All harvesters examined have the same size shown in **Fig.3.9**. To know the force

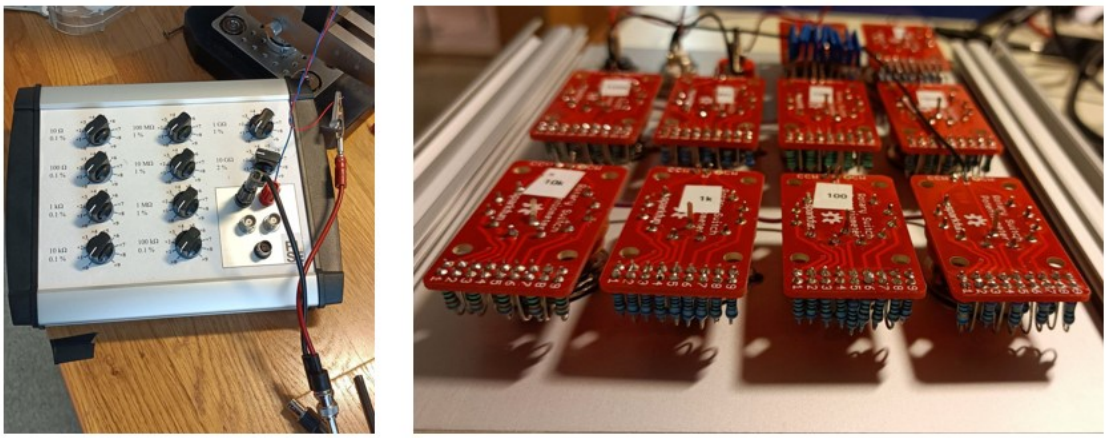

Figure 3.7: Box for the change of resistance, and resistors inside of it

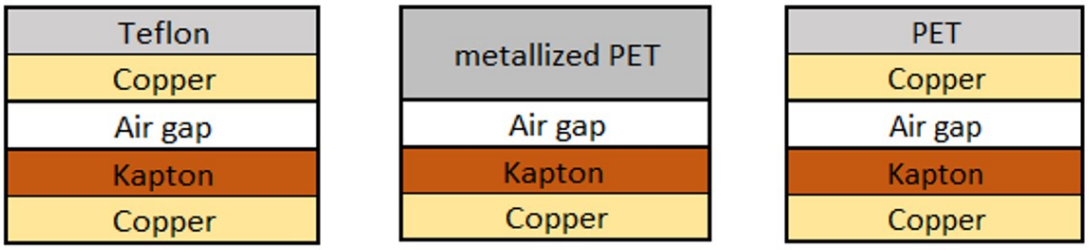

Figure 3.8: Configurations of the harvesters

	Kapton	Pet	Teflon	Air gap
Thickness $[mm]$	0.2	0.1	0.05	0.45
$\varepsilon_r[-]$	3.4	3.4	2	1

Table 3.1: Thickness and relative permittivity of the considered layers

applied also in case of tapping, or whenever there is not the possibility to have a force sensor connected, a PVDF harvester nr.4 from RISE was calibrated with the hammer, which is equipped with a load cell, hitting the harvester from higher and higher distance, the load cell will measure higher force as displayed in **Fig.A.1**, where the force measured has diffrent peak between 30 and 200 N. In this way, it is obtained a regression straight line between the voltage read from the RISE's PVDF and the force applied. The outcome of this study is depicted in **Fig.3.10** Although it is worth pointing out that the data are quite scattered, maybe it is due to the noise of the hammer and the environment. In this way, we can compare the voltage from PVDF and tribo harvesters only by tapping. In general, it can

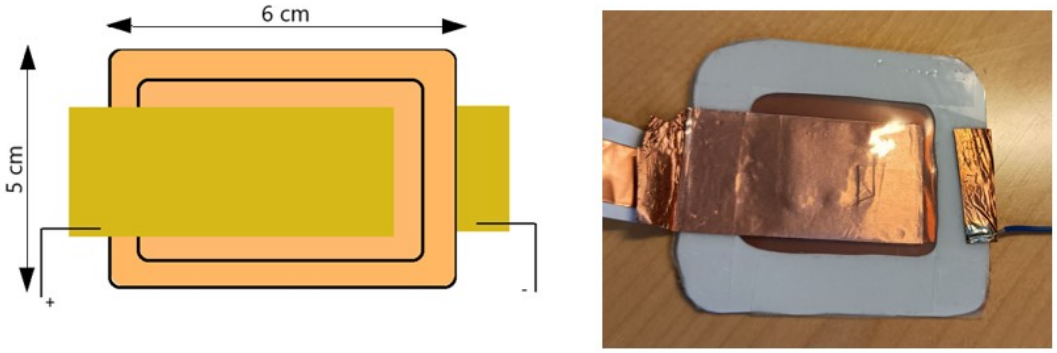

Figure 3.9: Size of the harvesters

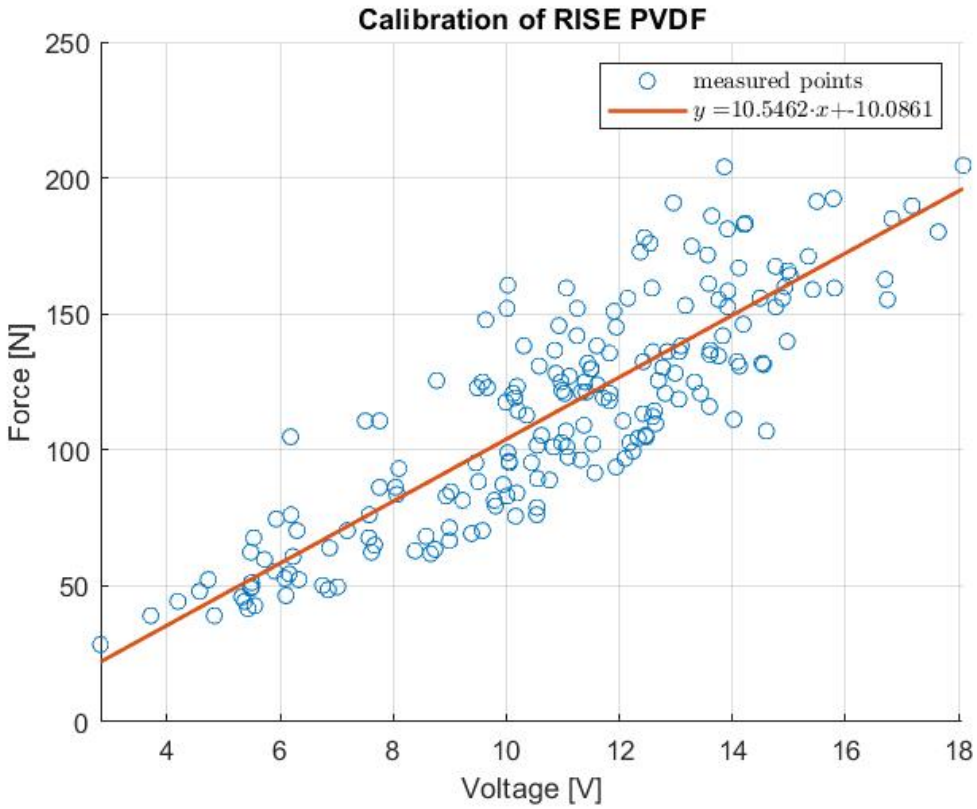

Figure 3.10: Calibration of RISE PVDF

be seen in **Fig.3.11** that PVDF has a higher voltage than tribo. Moreover, if the force decreases, both voltages will decrease.

Finally, in **Fig.3.12** it is noticed that changing the triboelectric material of the

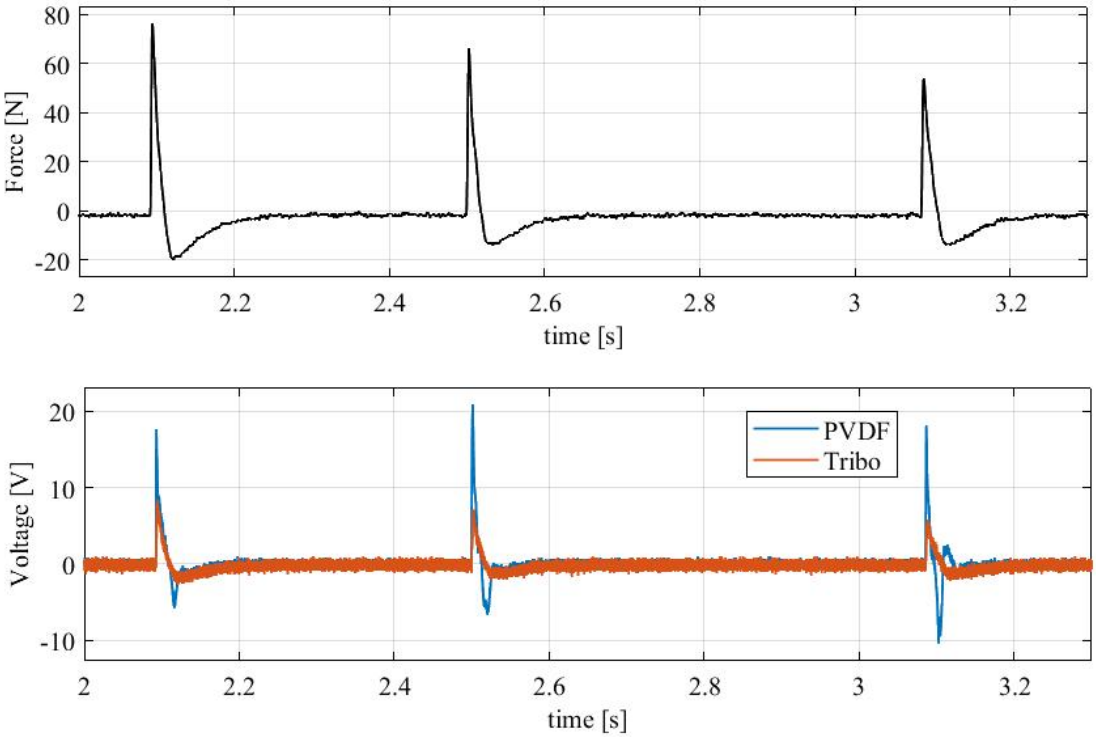

Figure 3.11: The voltage output of PVDF and triboelectric harvesters for the same applied force

harvester will result in a change in output.

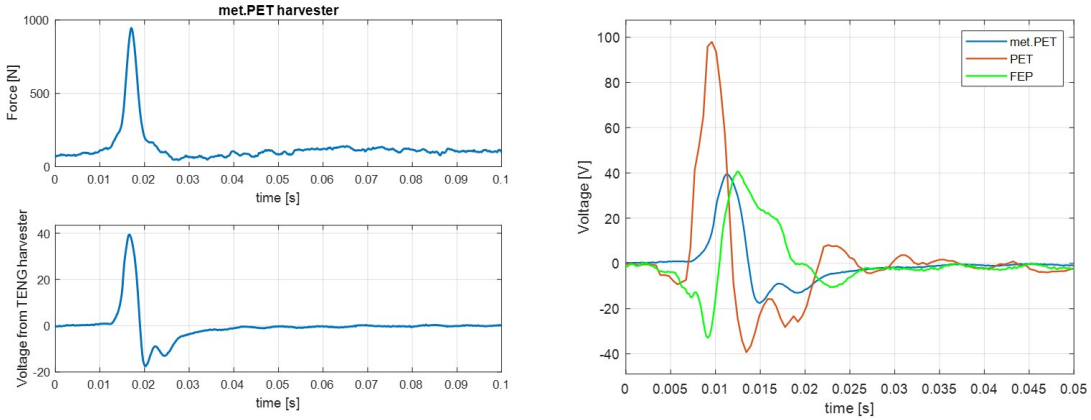

Figure 3.12: Voltage dependant on the materials applying the same force

The force can be considered impulsive since its peak has an amplitude of $10ms$, and the same trend is present in the voltage, although with different amplitudes and response times depending on the materials. In these experiments, It is not feasible to apply always the same force, although it is possible to stay in a small range of variation as in **Fig.3.13**, which is a statistic representing the probability of each hammer blow to be within one of the intervals of forces on the x-axis, in this case, $\pm 50N$ can be considered a good limit.

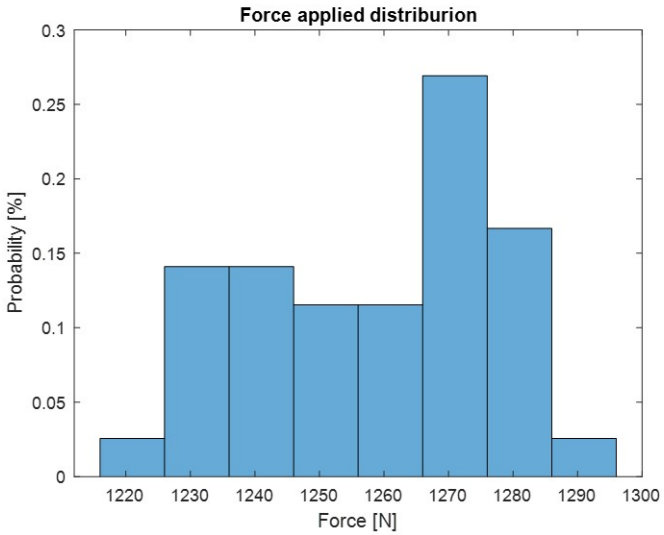

Figure 3.13: Forces applied in the hammer measurements

We see from **Fig.3.14** that, as expected, the voltage starts from 0 V and then increases with resistance, since it tends to an open circuit, where the maximum voltage occurs. In reverse, the current decreases, since at open-circuit (very high resistance) it tends to be null. These same results can be seen in **Fig.A.2** and **A.3**, indeed the signal has the charcteristic of an impulsive signal. Considering the power, in **Fig.3.15** as the product of current and voltage, there is a maximum of $0.6mW$ for the harvester with kapton and metallized PET, while, for the harvester with kapton and PET, the maximum power is lower ($0.5mW$).

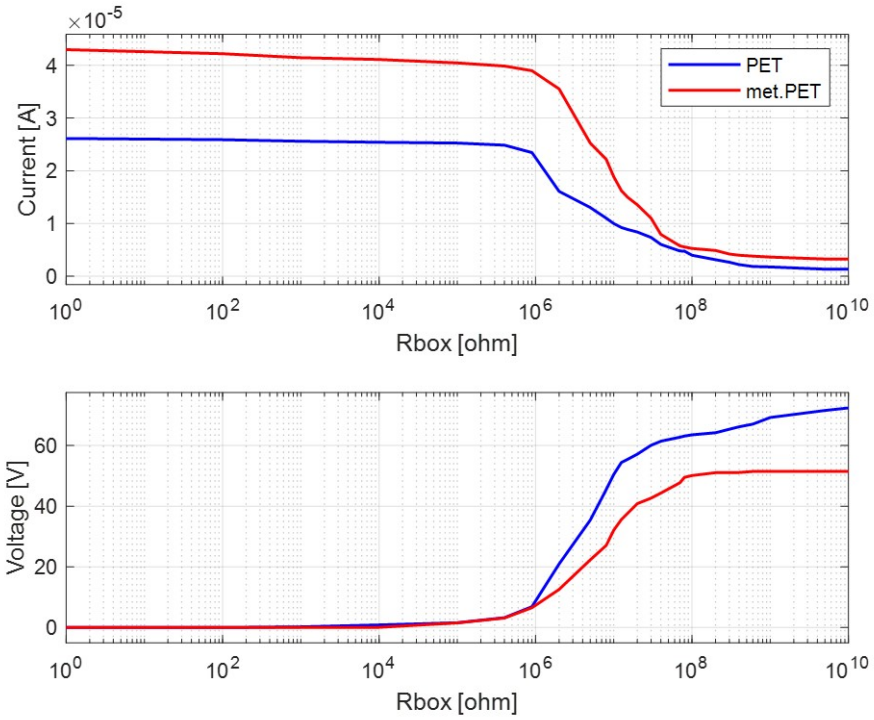

Figure 3.14: Current and voltage measured for each resistive load

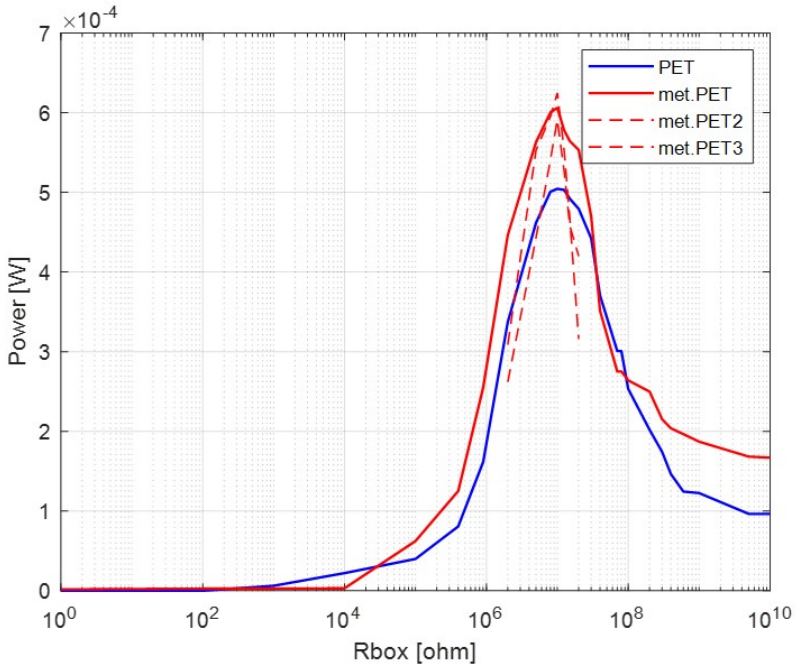

Figure 3.15: Power output for each resistive load

This means that having an active area of $2.5mm$ x $3.5mm$ there is a power density of:

$$P_d = \frac{6 \cdot 10^{-4} W}{2.5mm \cdot 3.5mm} = 0.778 \frac{W}{m^2} \tag{3.1}$$

Given that it is unrelated to the structure's surface, power density is a good measure to utilize when discussing the results. The value achieved in this study is less than many others compared to the findings reported in the literature (**Table 3.2**), but at least both the power density and the impedance where the maximum power is present are comparable.

Project	Materials	Impedance $[M\Omega]$	Power density $\frac{W}{m^2}$
This project	Kapton	10	0.778
Paranjape et al.	PDMS	50	4
Sukumaran et al.	Recycled Kapton	100	0.16
Singh et al.	Kapton/PVDF	120	0.245

Table 3.2: Comparison with the literature results

Although different materials and design of the structure are used.

In Paranjape et al.[24], it is used a (3D) printed bidirectional rotatory hybrid nanogenerator made of a composite film of NaNbO3/PDMS. Indeed, they used particles of NaNbO3, which is a ceramic materials with high dielectric constant to enhance the dielectric constant of the PDMS. Moreover, they used six TENG together, and they worked on the gap variation instead of the gap.

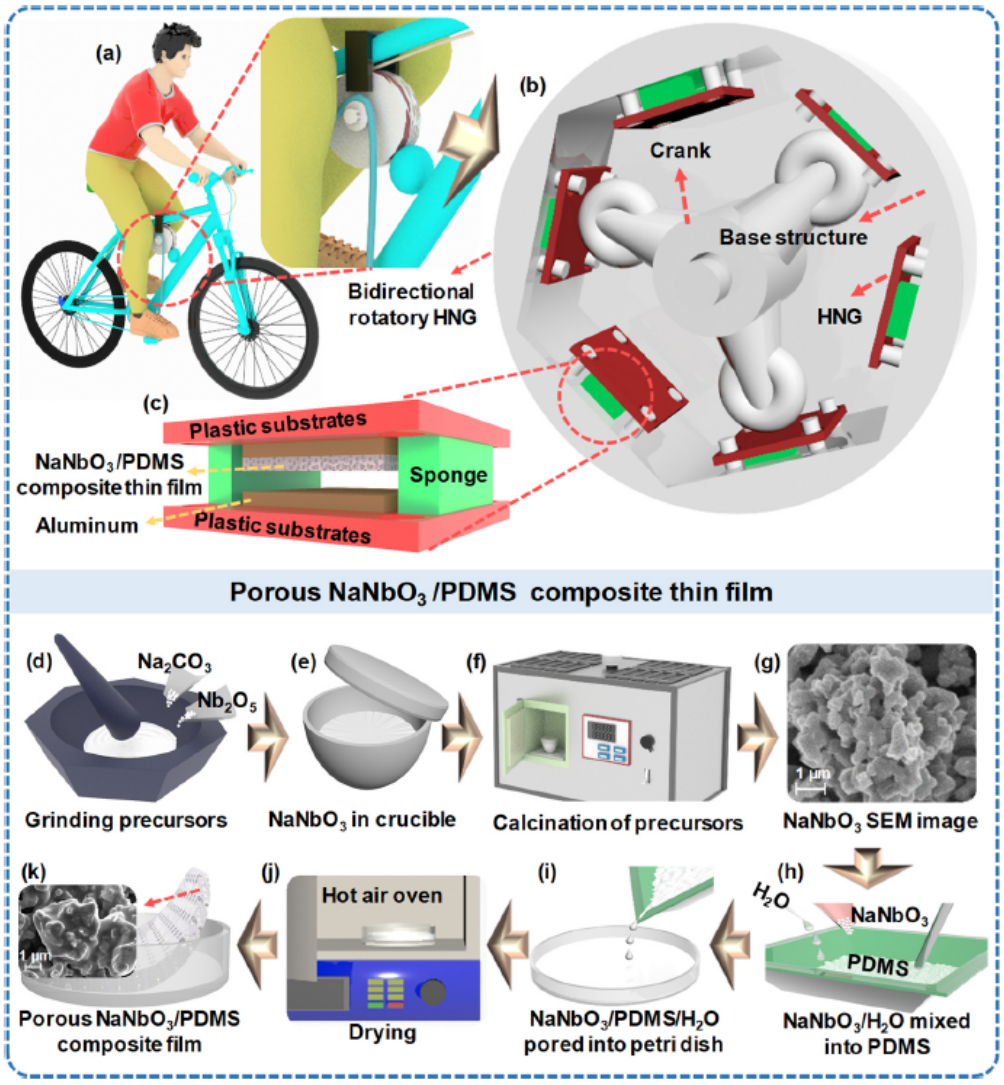

Figure 3.16: Schematic drawing of the nanogenerator presented by [24] and chemical production of the NaNbO3/PDMS dielectric layer.

The way of excitation is different, it is used three crankheads compressing the TENG, instead of bending or tapping. In Sukumaran et al.[16], it is illustrated an EYE-TENG (because of the oval eye shape) which uses recycled PET acting as the substrate for the triboelectric active layers in the device.

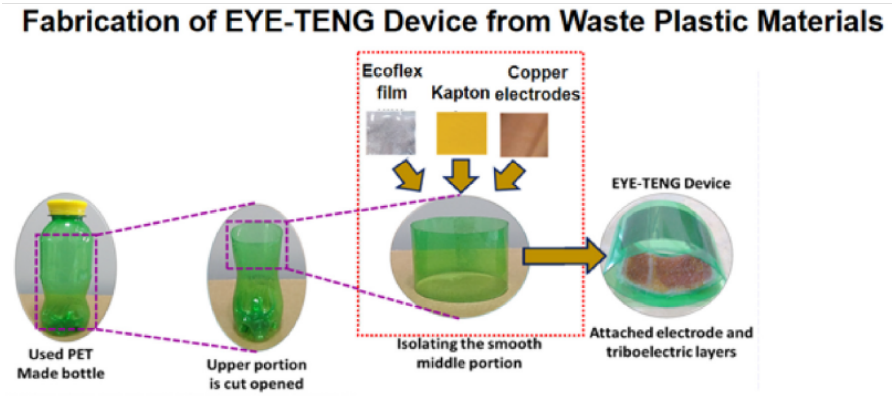

Figure 3.17: Fabrication process of the EYE-TENG in [16]

They got higher voltage and current values than the ones in this thesis project because there is higher distance between the layers, even though edge effects could appear and the open circuit voltage could deviate from the linearity with the air gap. Moreover this structure is not applicable in car tires since it will not feel the bending of the tire. On the contrary the configuration illustrated in this project does not allow the complete contact of the layers.

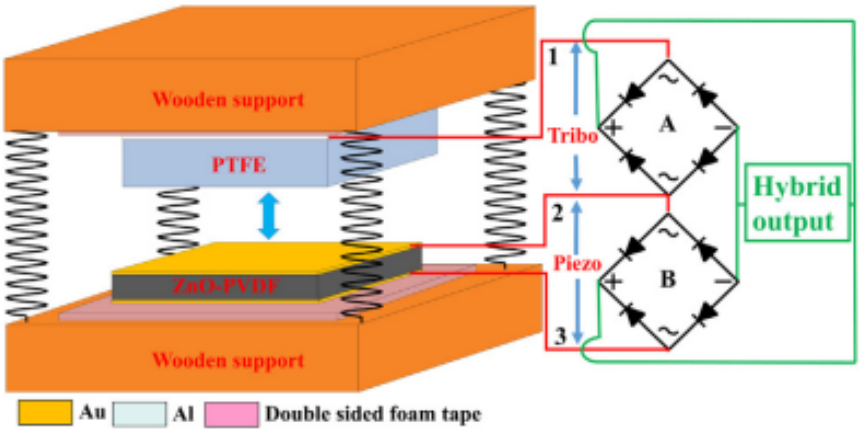

Figure 3.18: Sketch of hybrid nanogenerator and circuit with rectifiers from [25].

In Singh et al.[25] an hybrid nanogenerator is analysed. It exploits both the piezoelectric effect from PVDF and the triboelectric effect from PTFE and PVDF. Some nanorods of Zn0 are inserted in the PVDF with a result of enhancing its triboelectric and piezoelectric properties, another effect of the insertion of ZnO is that the surface roughness increases as well as the contact area, consequently. In

addition they use aluminum and gold electrodes instead of copper which is more oxidable than gold. This device is then connected to two bridge rectifiers (each one for tribo and piezo) to convert AC current to DC.

3.4 Shaker test

To measure the voltage and current in the frequency, a wave generator is needed that provides a square wave with 800 mV of amplitude (the maximum applicable is 1.2 V), 50% of duty cycle to have a symmetric wave. This is amplified in current and goes to the actuator. It is made by a solenoid, the current passes through the coils, and there is a displacement cylinder to have the tapping on TENG. To know the applied force, there is the PVDF that was calibrated before. This setup is shown in **Fig.3.19**

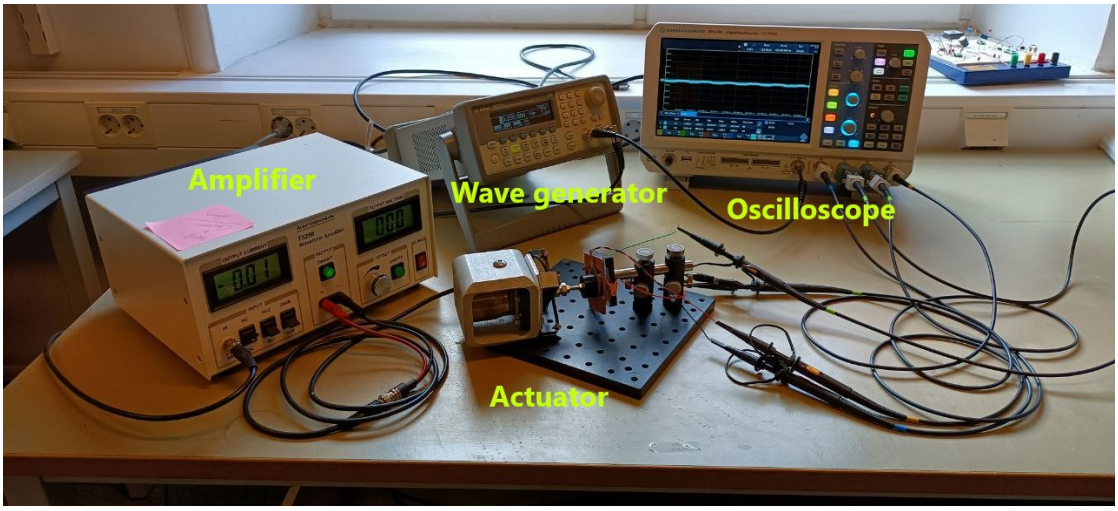

Figure 3.19: Power output for each resistive load

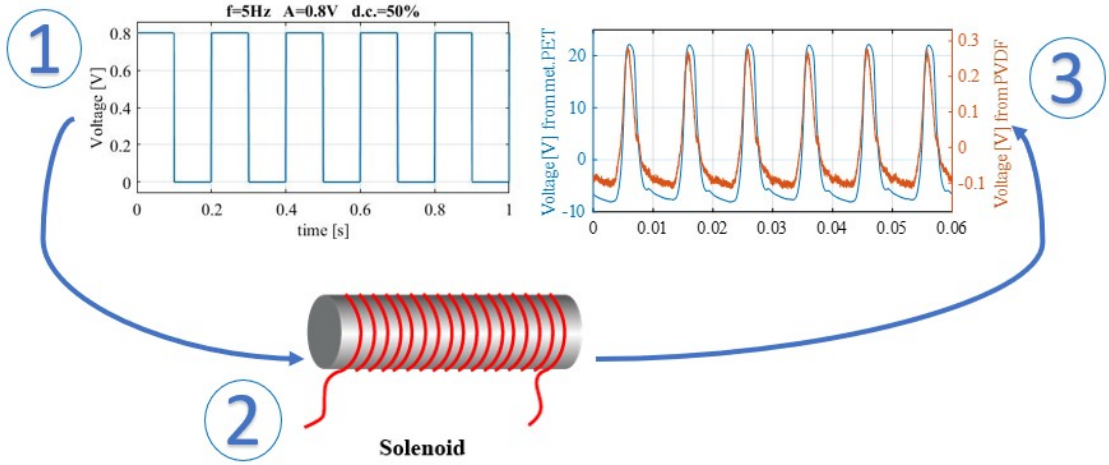

Figure 3.20: Working scheme of the shaker

This method of making experiments is extraordinarily reliable because it produces extremely reproducible signals in (**Fig.3.20**), where a square wave of 6 Hz of frequency and 0.8 V of amplitude turns out in a signal with 22 V and -10V of positve and negative peak from the TENG (blue) in the face of a force (voltage from PVDF in red) almost 3N. As shown in **Fig.3.10** the angular coefficient is 10.56 N/V.

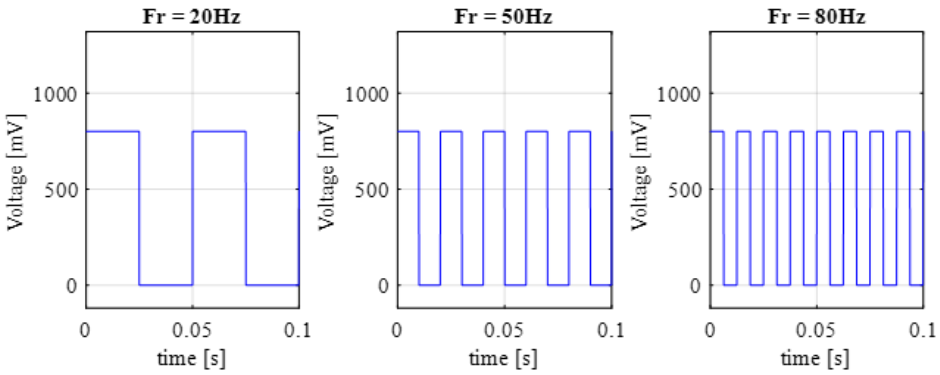

Figure 3.21: Square wave applied to have the results in **Fig.3.22**

In **Fig.3.21** it is reported square wave (as example at 20, 50, 80 Hz) generated and applied to have the frequency variation results.

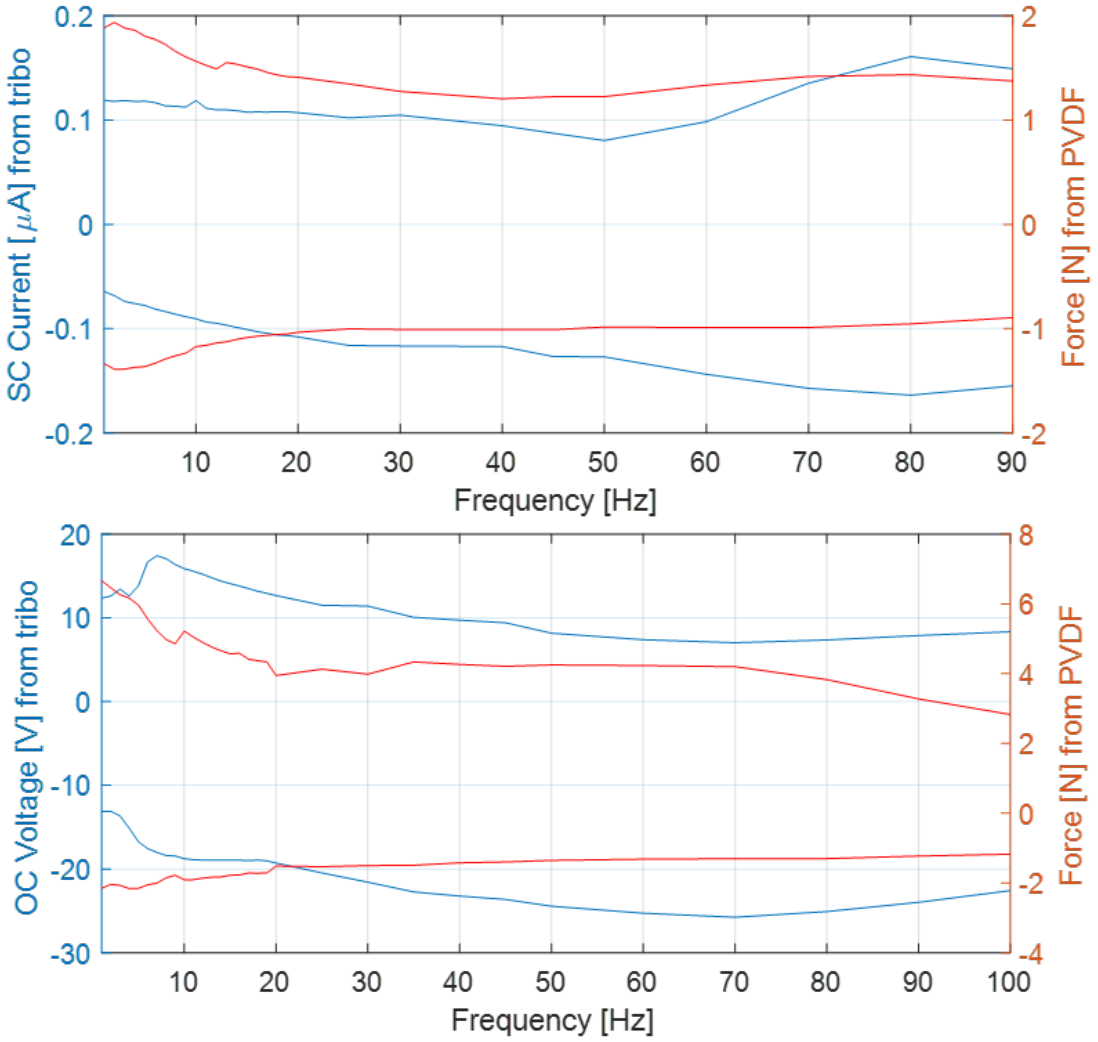

Figure 3.22: Positive and negative peak of the voltage and current vs amplitude of the square wave

Having applied the same amplitude (850 mV) in **Fig.3.22**, regarding the short circuit measurements, it is mainly constant as well as the force measured from piezoelectric, whereas the open circuit voltage has a peak at more or less 8 Hz in the positive peak of the voltage.

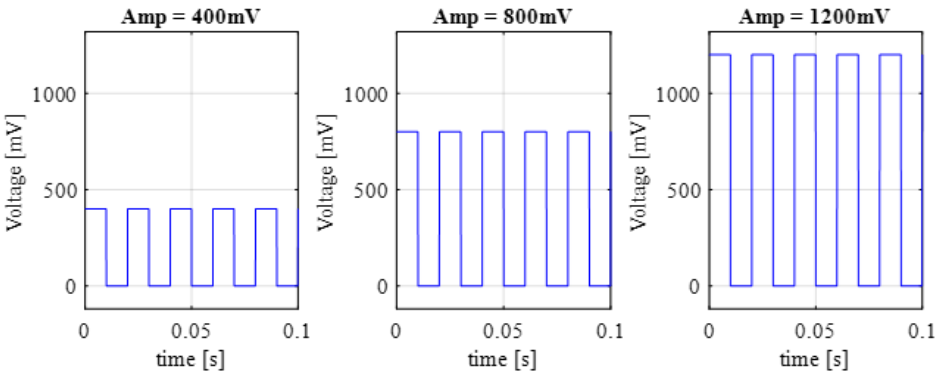

Figure 3.23: Square wave applied to have the results in **Fig.3.24**

In **Fig.3.23** it is reported the square wave generated to have the result in **Fig.3.24**. The frequency is kept constant at 5 Hz, and changing the amplitude of the square wave (as example 400, 800 1200 mV). Similar conclusions can be drawn for both open circuit voltage and short circuit current:

- Increase of amplitude produces increase of force, same for voltage and current, with almost 4 N, there are 20 V and 0.28 μA
- In correspondence of 1200 mV of amplitude there is a kind of saturation (tendency to remain constant) at 20 V for voltage and 0.28 μA

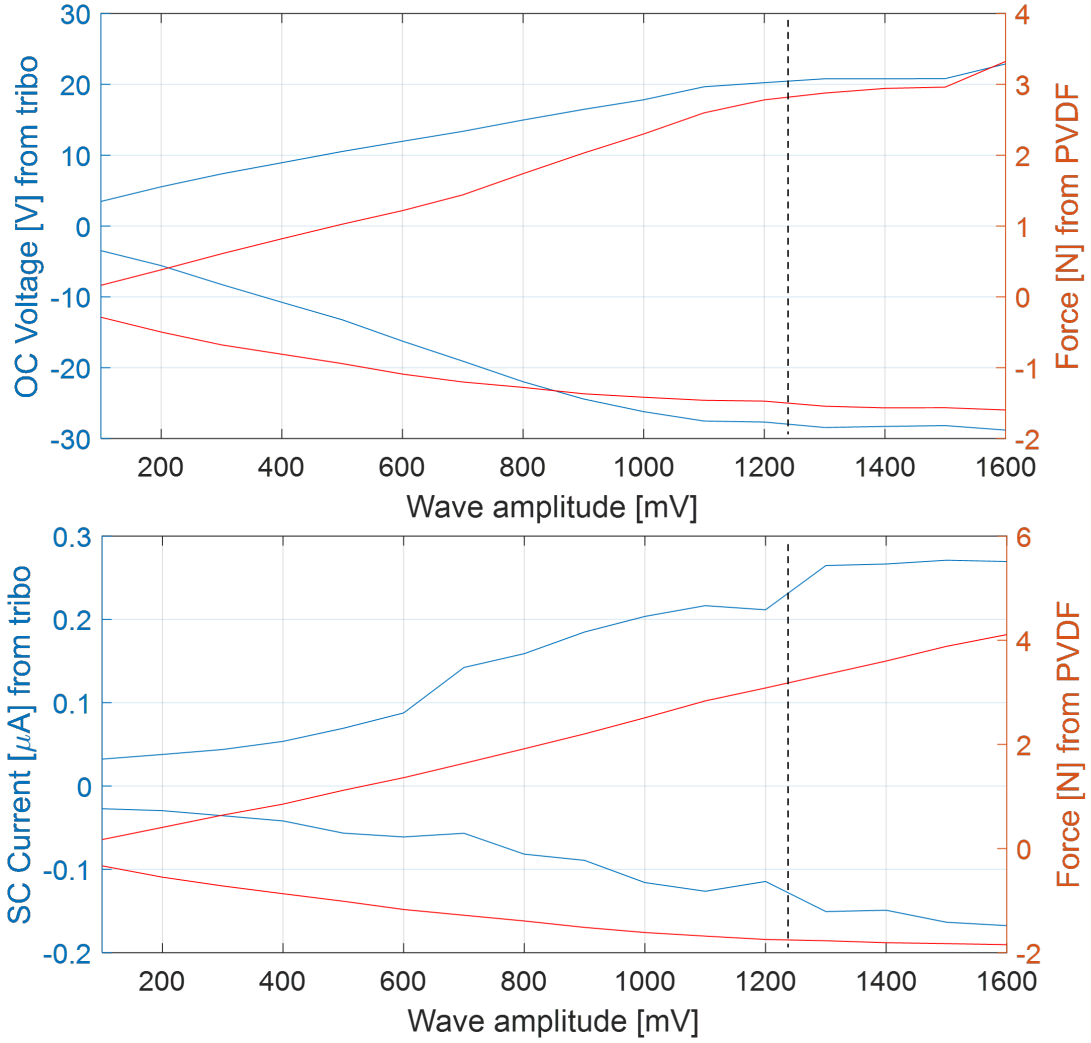

Figure 3.24: Positive and negative peak of the voltage and current vs frequency of the square wave

Chapter 4

Nokian Tyres experiments

The aim of the following experiments is testing the TENG in a condition closer to the real final application in a vehicle tire. These experiments were performed at the Nokia Test center of Nokian Tyres in Finland.

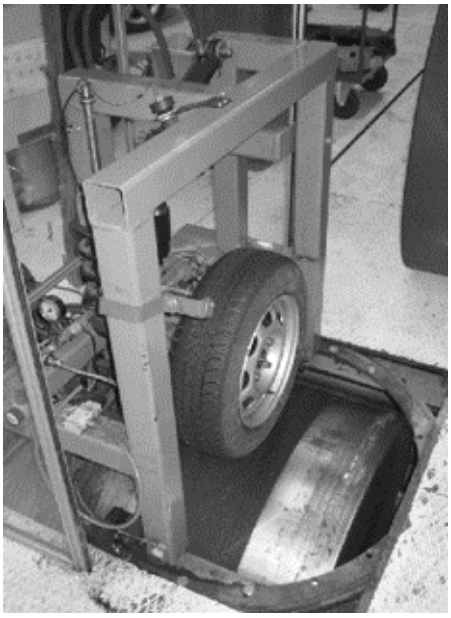

(a) Test rig to simulate the car load

(b) Position of the tribo harvester in the tire from Nokian Tyres

Figure 4.1: Nokian set up

The tire is put on a cylindrical drum and kept in contact with it by the test rig (**Fig.4.1a**) which applies a load of 3000 N, it can be considered as one quarter of the total weight of a car. The drum rotates at constant speed which is changed

for each measurement (10, 20, 30, 70, 90 km/h). The outputs measured are in displayed in **Fig.A.4** and **Fig.A.5**, where reducing the timespan to 1s, it is possible to understand better the signals. The TENG is attached on the inner surface of the tire by means of a double sided tape. And, an extra protective duct tape (in black) is added to have more protection and avoid a relative displacement with respect the tire surface. Nr.5 and Nr.6 **Fig.4.1b**) denote respectively the tribo met.PET and the tribo PET. Both of them have been measured,

Afterwards, the measured open circuit voltage and short circuit current are transferred to the database by means of a BLE (Bluetooth Low Energy) device, which is supported in MATLAB, and can allow to scan peripheral device and to avoid the installation of wires or cables into the tire from the outside. It is convenient to place the harvester in the middle of the tire inner surface, indeed it is where there is the maximum displacement in **Fig.4.2**

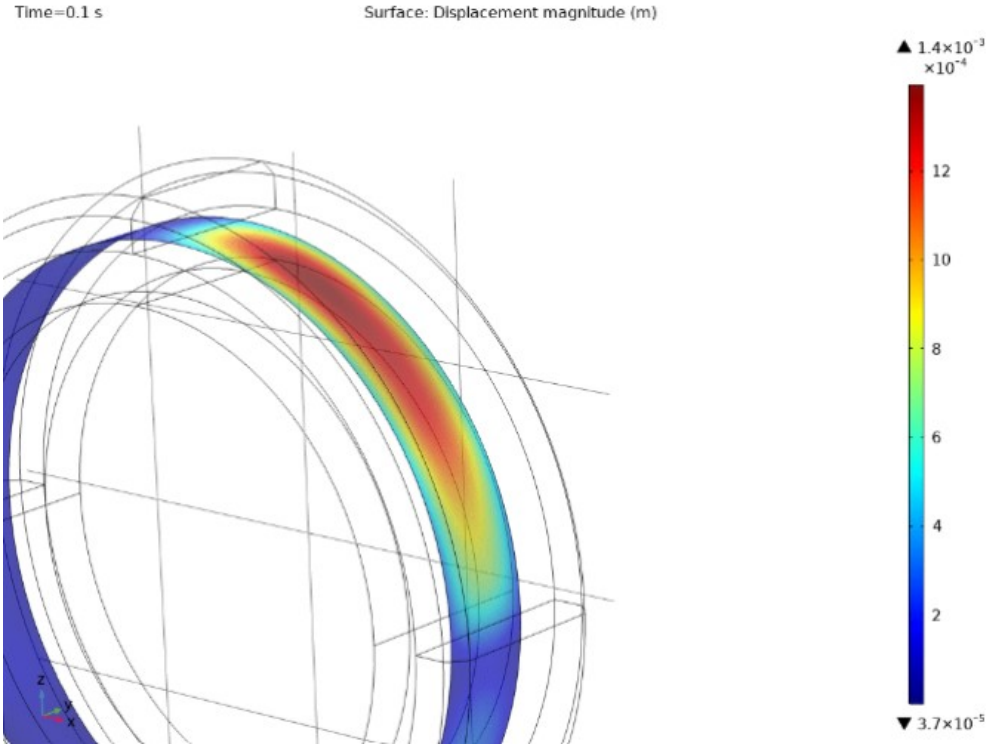

Figure 4.2: Displacement of the inner surface of the tire.

It is an extremely simplified model, considering the tire made by an isotropic material with elastic modulus $E = 15\ MPa$ (an estimation was made in [26]) and Poisson coefficient $\nu = 0.3$. Then, this rubber layer surrounds the inner rim made

of structural steel. Morover the real tire has a "toroidal shape" instead of being cylindrical with flat contact surface, and in a real vehicle, the tires are not often perpendicular to the terrain. And applying a moving load of 3000 N on region large 10 cm perpendicularly to the thread of the tire. Nevertheless, this model it is useful to have a rough estimation, at least from the qualitative point of view that the highest displacement (1.2 mm) is located in the middle of the tire.

In the following sections are reported only the measurements done with the tribo met.PET, which are more clear and less noisy than the ones about the tribo PET.

4.1 Voltage measurements

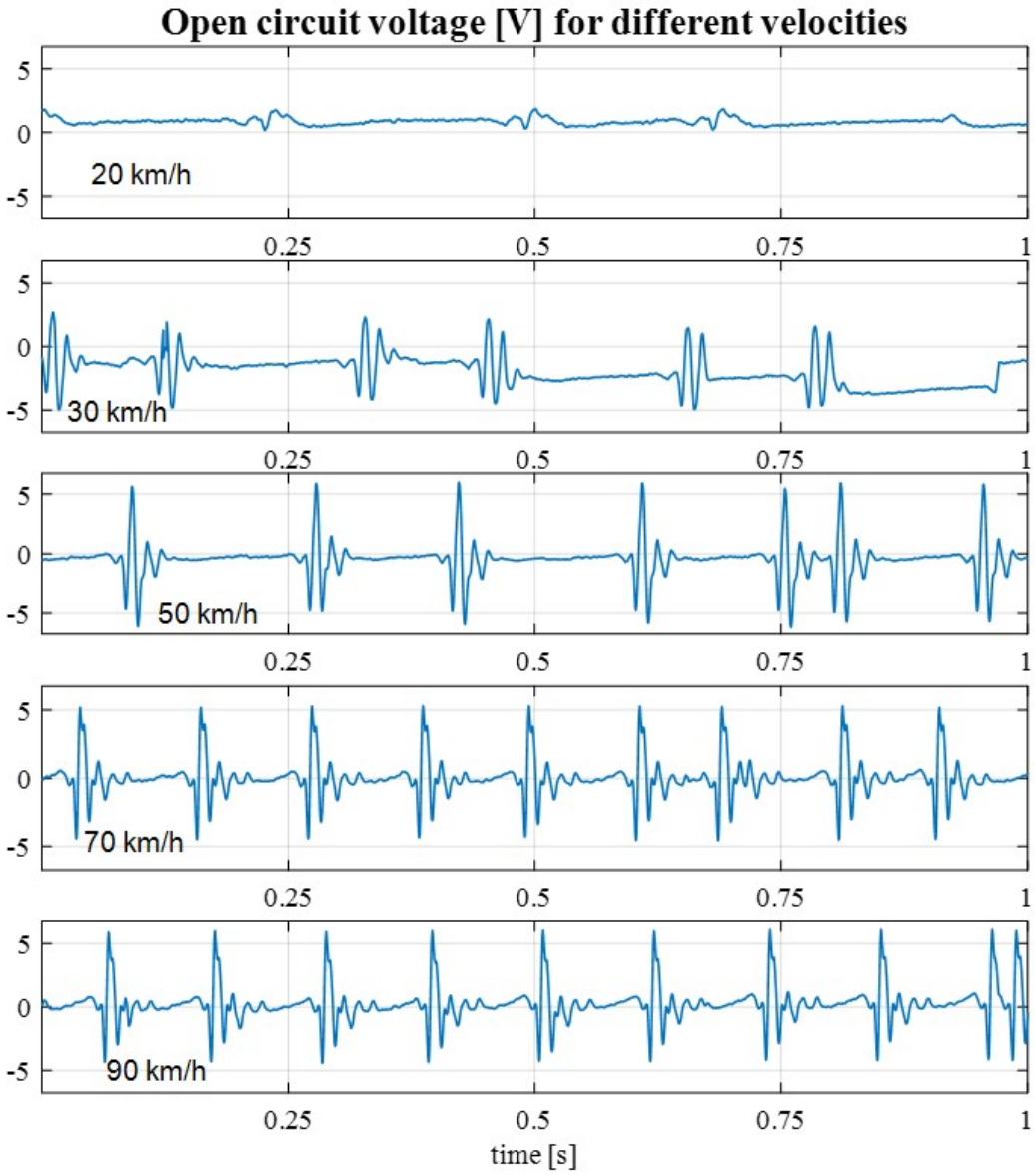

Figure 4.3: Voltage measurements for different velocities

From the chart in **Fig.4.3**, at 20 km/h, the open circuit voltage is too small to be considered useful to feed an electric load, the velocity needs to be at least 30 km/h where there are $\pm$ 3 V, it is clear that the velocity increased because the frequency of the signal is higher. Next, for 50 and 70 km/h the amplitude

of voltage is constant at 5 V. Finally, at 90 km/h there is the maximum value of voltage, almost 6 V.

4.2 Current measurements

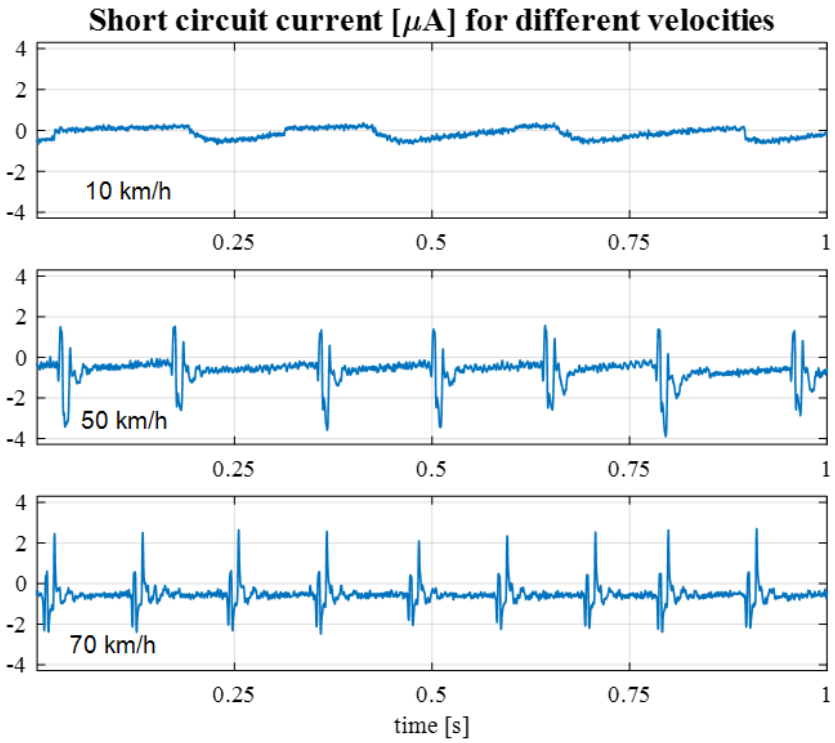

Figure 4.4: Current measurements for different velocities

Same considerations made for voltage are valid for the current in **Fig.4.4**, even if only three velocities are good measurements while in the others, there were some difficulties during the test, reaching 2 μA, it is conceivable that the current, at 90 km/h, could reach even slightly higher values. From these charts, the frequency in very low, provided that the tire tested has a radius of 16":

$$f = \frac{\frac{70km/h}{3.6}}{2\pi \cdot \left(2.54 \cdot \frac{16cm}{100}\right)} = 9Hz \tag{4.1}$$

Meaning that in each second there are 9 cycles as in **Fig.4.4**

4.3 Result comparison

In this section, the goal is to estimate what is the force felt by the harvester when the tire rotates. Thus, the harvester can work as a sensor to get an insight about the tire condition, such as wear, pressure and forces. The results got from the nokian test will be compared with the results from RISE experiments. To do

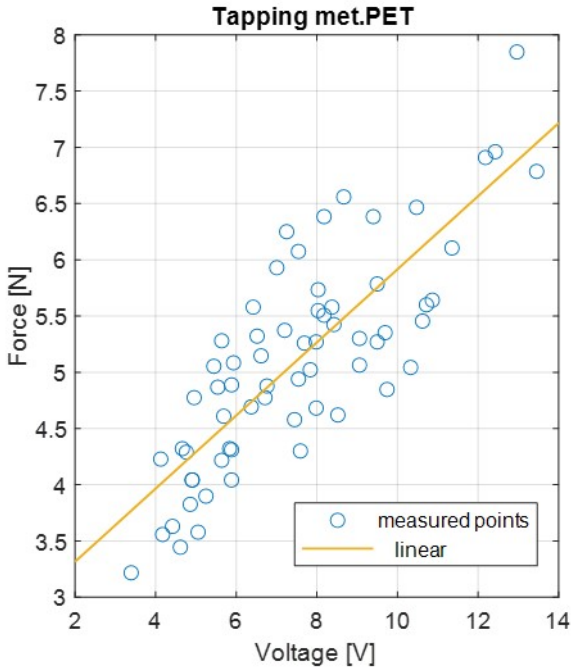

Figure 4.5: Force vs open circuit voltage calibration

this, the PVDF is attached underneath the TENG, therefore it is possible to detect the force applied by tapping (PVDF has been already calibrated), then, the open circuit voltage from TENG is measured. In this way, it is possible to identify a linear relationship between the open circuit voltage and force (**Fig.4.5**), this is Force vs Voltage calibration.

Speed $[km/h]$	**Voltage** $[V]$	**Force** $[N]$
20	0.8	2.28
30	1.2	2.76
50	5	4.4
90	6	5.2

Table 4.1: Estimation of the force at each tire speed

These results are to be taken only as a qualitative reference due to the presence many uncertainties (i.e. hammer and environment noise), and there are no similar results in literature to be compared with. Now it is possible to have a first estimation of the force at each tire speed in **Tab.4.1**. These are very low values of force and are to be taken only as a qualitative reference due to the presence many uncertainties (i.e. hammer and environment noise), and there are no similar results in literature to be compared with. However the harvester is capable to produce enough power to feed some electrical loads.

Chapter 5

Conclusions and future perspectives

Triboelectric energy harvesting is an attractive technology because of its high power density, ease to manufacturing, and undeniable versatility. Indeed, a TENG can harvest mechanical energy from a multitude of sources, for example, in wave energy converters, and its earliest application was in wearable electronics to harvest human body motion. The most recent application is in automotive tires, although it is still in the stage of academic research and only few companies are investigating its usage.

The physics behind the triboelectric effect has been discussed, and the different way of deploying the triboelectric charges in energy harvesting has been shown depending on the choice of material as dielectric layer. As well as the main four working mode have been presented with their pros and cons. Particular interest and effort is put in the numerical model and experimental analysis of the TENG in vertical contact mode.
In particular, the electrostatic behavior of the lateral sliding mode and the vertical contact mode has been simulated in the FEM software COMSOL Multiphysics. From this latter model there is a maximum stress of 75 MPa which is below the yielding stress values of the material involved ($100 \div 150$ MPa), considering also that in the model there is no stiffer substrate representing the tire, indeed the displacement is higher, but, consequently, the stress as well is higher than the real case. The model with both electrostatics and solid mechanics is too time consuming, meaning that COMSOL it is not optimised to deal with a moving load in a simulation with electrostatic and mechanics, furthermore does not exist an

interface (as it is for piezoelectric) to simulate in detail the triboelectric effect. In the future many improvements are needed to have further numerical results regarding the triboelectric nanogenerator. A PVDF sample was calibrated in order to have the possiblity to know the force applied and felt by the TENG, and the possibility to produce current and voltage when the TENG is bent was proved using the MARK10 instrument. Then,a characterisation of the harvester was made to identify the profile of power, current and voltage. The result is that the maximum power density is 0.8 mW, which is located at 10 $M\Omega$, this is the internal resistance of the TENG. The TENG have been tested on a real tire. In comparison to slower speeds, higher speeds also result in shorter peaks (contact with the ground). As a result, each rotation's available energy essentially stays the same while slightly increasing at greater speeds. As the speed rises, the energy output per second rises. In light of this, it may be concluded that driving the car faster (up to a specific top speed) is energy beneficial, at least over 70 km/h.

After this thesis, it is clear that the future for triboelectric energy harvesting is bright, nevertheless further experiments are needed on the way to characterise the sensoristic properties of TENGs. An hybrid nanogenerator is going to be implemented in tires to harvest mechanical energy from piezoelectric and triboelectric effects at the same time. Regarding the testing development, the TENG has to be tested on a real vehicle driven on a real road.

Bibliography

[1] Zhong Lin Wang and Aurelia Chi Wang. "On the origin of contact-electrification". In: *Materials Today* 30 (2019), pp. 34–51. ISSN: 1369-7021. DOI: https://doi.org/10.1016/j.mattod.2019.05.016. URL: https://www.sciencedirect.com/science/article/pii/S1369702119303700 (cit. on p. 2).

[2] Weon-Guk Kim, Do-Wan Kim, Il-Woong Tcho, Jin-Ki Kim, Moon-Seok Kim, and Yang-Kyu Choi. "Triboelectric Nanogenerator: Structure, Mechanism, and Applications". In: *ACS Nano* 15.1 (2021). PMID: 33427457, pp. 258–287. DOI: 10.1021/acsnano.0c09803. eprint: https://doi.org/10.1021/acsnano.0c09803. URL: https://doi.org/10.1021/acsnano.0c09803 (cit. on p. 2).

[3] *Van De Graaff Generator*. Sept. 2022. URL: https://en.wikipedia.org/wiki/Van_de_Graaff_generator (cit. on p. 4).

[4] Hannah Ritchie, Max Roser, and Pablo Rosado. "Energy". In: *Our World in Data* (2020). https://ourworldindata.org/energy (cit. on p. 5).

[5] Zhong Lin Wang, Long Lin, Jun Chen, Simiao Niu, and Yunlong Zi. "Triboelectrification". In: *Triboelectric Nanogenerators*. Cham: Springer International Publishing, 2016, pp. 1–19. DOI: 10.1007/978-3-319-40039-6_1. URL: https://doi.org/10.1007/978-3-319-40039-6_1 (cit. on p. 5).

[6] Enrique Delgado-Alvarado, Ernesto A Elvira-Hernández, José Hernández-Hernández, Jesús Huerta-Chua, Héctor Vázquez-Leal, Jaime Martınez-Castillo, Pedro J Garcıa-Ramırez, and Agustın L Herrera-May. "Recent Progress of Nanogenerators for Green Energy Harvesting: Performance, Applications, and Challenges". In: *Nanomaterials* 12.15 (2022), p. 2549 (cit. on p. 6).

[7] Jino Ramson. "Applications of wireless sensor networks — A survey". In: Nov. 2017. DOI: 10.1109/ICIEEIMT.2017.8116858 (cit. on p. 8).

[8] Venkateswaran Vivekananthan, Arunkumar Chandrasekhar, Nagamalleswara Rao Alluri, Yuvasree Purusothaman, Gaurav Khandelwal, and Sang-Jae Kim. "Triboelectric Nanogenerators: Design, Fabrication, Energy Harvesting, and Portable-Wearable Applications". In: *Nanogenerators*. Ed. by Sang Jae Kim, Arunkumar Chandrasekhar, and Nagamalleswara Rao Alluri. Rijeka: IntechOpen, 2020. Chap. 1. DOI: 10.5772/intechopen.90951. URL: https://doi.org/10.5772/intechopen.90951 (cit. on pp. 8, 9).

[9] Zhong Lin Wang, Long Lin, Jun Chen, Simiao Niu, and Yunlong Zi. "Triboelectric Nanogenerator: Vertical Contact-Separation Mode". In: *Triboelectric Nanogenerators*. Cham: Springer International Publishing, 2016, pp. 23–47. ISBN: 978-3-319-40039-6. DOI: 10.1007/978-3-319-40039-6_2. URL: https://doi.org/10.1007/978-3-319-40039-6_2 (cit. on pp. 9, 23, 24).

[10] Zhihao Zhao et al. "Selection rules of triboelectric materials for direct-current triboelectric nanogenerator". In: *Nature Communications* 12 (Aug. 2021). DOI: 10.1038/s41467-021-25046-z (cit. on p. 10).

[11] Haiyang Zou et al. "Quantifying the triboelectric series". In: *Nature Communications* 10 (Mar. 2019). DOI: 10.1038/s41467-019-09461-x (cit. on p. 11).

[12] Satish Kumar, Rajeev Kumar, Wolfgang Seemann, and Satish Chandra Jain. "Modeling and Analysis of Vertical Contact Mode Triboelectric Energy Harvester". In: *Integrated Ferroelectrics* 212.1 (2020), pp. 68–80. DOI: 10.1080/10584587.2020.1819036. eprint: https://doi.org/10.1080/10584587.2020.1819036. URL: https://doi.org/10.1080/10584587.2020.1819036 (cit. on pp. 12, 13).

[13] Xiaoliang Cheng, Wei Tang, Yu Song, Haotian Chen, Haixia Zhang, and Zhong Lin Wang. "Power management and effective energy storage of pulsed output from triboelectric nanogenerator". In: *Nano Energy* 61 (2019), pp. 517–532. ISSN: 2211-2855. DOI: https://doi.org/10.1016/j.nanoen.2019.04.096. URL: https://www.sciencedirect.com/science/article/pii/S2211285519303970 (cit. on pp. 14, 16).

[14] Simiao Niu, Yu Sheng Zhou, Sihong Wang, Ying Liu, Long Lin, Yoshio Bando, and Zhong Lin Wang. "Rapid communication". English. In: *Nano Energy* 8.Complete (2014), pp. 150–156. DOI: 10.1016/j.nanoen.2014.05.018 (cit. on p. 15).

[15] Shaojun Zhang, Ye Wu, Huan Liu, Ruikun Huang, Puikei Un, Yu Zhou, Lixin Fu, and Jiming Hao. "Real-world fuel consumption and CO2 (carbon dioxide) emissions by driving conditions for light-duty passenger vehicles in China". In: *Energy* 69 (2014), pp. 247–257. ISSN: 0360-5442. DOI: https://doi.org/10.1016/j.energy.2014.02.103. URL: https://www.sciencedirect.com/science/article/pii/S0360544214002503 (cit. on p. 15).

[16] Charanya Sukumaran, Venkateswaran Vivekananthan, Velumani Mohan, Zachariah C. Alex, Arunkumar Chandrasekhar, and Sang-Jae Kim. "Triboelectric nanogenerators from reused plastic: An approach for vehicle security alarming and tire motion monitoring in rover". In: *Applied Materials Today* 19 (2020), p. 100625. ISSN: 2352-9407. DOI: https://doi.org/10.1016/j.apmt.2020.100625. URL: https://www.sciencedirect.com/science/article/pii/S2352940720300731 (cit. on pp. 15, 41, 42).

[17] Ehsan Hashemi, Amir Khajepour, Mir Khamesee, and Zhong Wang. "Tire Condition Monitoring and Intelligent Tires Using Nanogenerators Based on Piezoelectric, Electromagnetic, and Triboelectric Effects". In: *Advanced Materials Technologies* 4 (Aug. 2018), p. 1800105. DOI: 10.1002/admt.201800105 (cit. on p. 16).

[18] Paolo Mazzoldi. *Fisica / P. Mazzoldi, M. Nigro, C. Voci*. ita. Napoli: S.E.S (cit. on p. 17).

[19] Simiao Niu, Ying Liu, Sihong Wang, Long Lin, Yu Sheng Zhou, Youfan Hu, and Zhong Lin Wang. "Theory of sliding-mode triboelectric nanogenerators". In: *Advanced materials* 25.43 (2013), pp. 6184–6193 (cit. on pp. 19, 20, 22).

[20] *Research Institutes of Sweden*. URL: https://www.ri.se/en/about-rise/about-rise (cit. on p. 29).

[21] *Kapton HN thermal insulating film, 304mm x 200mm x 0.075mm*. URL: https://my.rs-online.com/web/p/plastic-film/5363968?sra=pmpn (cit. on p. 29).

[22] *Why you should care about oscilloscope trigger system basics*. Aug. 2016. URL: https://www.electronicdesign.com/technologies/test-measurement/article/21801795/why-you-should-care-about-oscilloscope-trigger-system-basics (cit. on p. 30).

[23] "Data Collection And Analysis Software". In: (). URL: https://mark-10.com/products/software/ (cit. on p. 32).

[24] Mandar Vasant Paranjape, Sontyana Adonijah Graham, Harishkumarreddy Patnam, Punnarao Manchi, and Jae Su Yu. "3D printed bidirectional rotatory hybrid nanogenerator for mechanical energy harvesting". In: *Nano Energy* 88 (2021), p. 106250. ISSN: 2211-2855. DOI: https://doi.org/10.1016/j.nanoen.2021.106250. URL: https://www.sciencedirect.com/science/article/pii/S221128552100505X (cit. on pp. 40, 41).

[25] Huidrom Hemojit Singh and Neeraj Khare. "Flexible ZnO-PVDF/PTFE based piezo-tribo hybrid nanogenerator". In: *Nano Energy* 51 (2018), pp. 216–222. ISSN: 2211-2855. DOI: https://doi.org/10.1016/j.nanoen.2018.06.055. URL: https://www.sciencedirect.com/science/article/pii/S2211285518304506 (cit. on p. 42).

[26] B. Setiyana, C. Prabowo, J. Jamari, R. Ismail, S. Sugiyanto, and E. Saputra. "Numerical investigation of the hardness of tire rubber material by indentation method". In: *Journal of Physics: Conference Series* 1517.1 (Apr. 2020), p. 012020. DOI: 10.1088/1742-6596/1517/1/012020. URL: https://dx.doi.org/10.1088/1742-6596/1517/1/012020 (cit. on p. 49).

Appendix A

Appendix

A.1 RISE Experiments

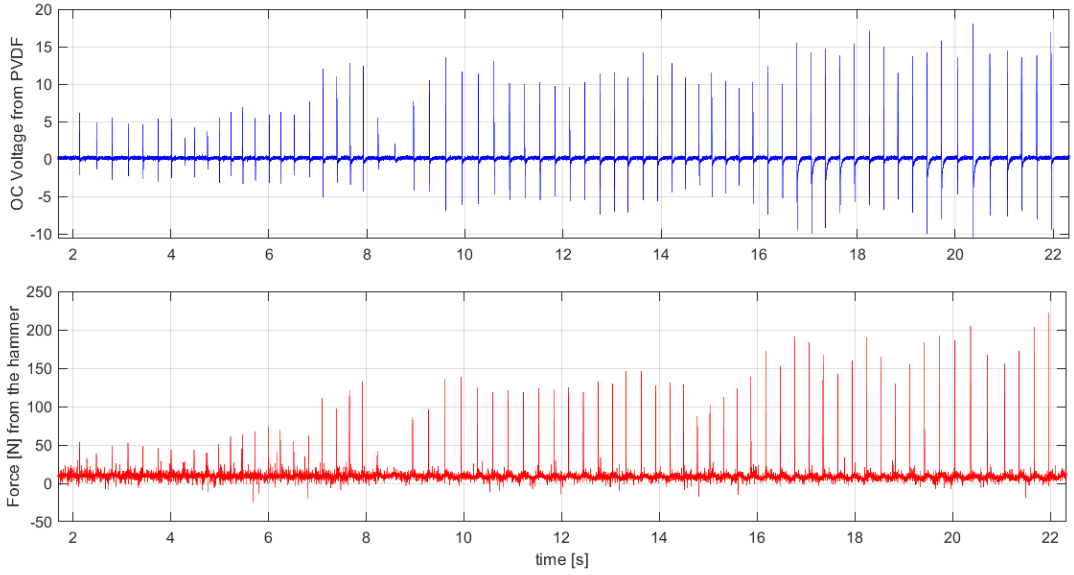

Figure A.1: Measurements with the hammer to calibrate the PVDF nr.4

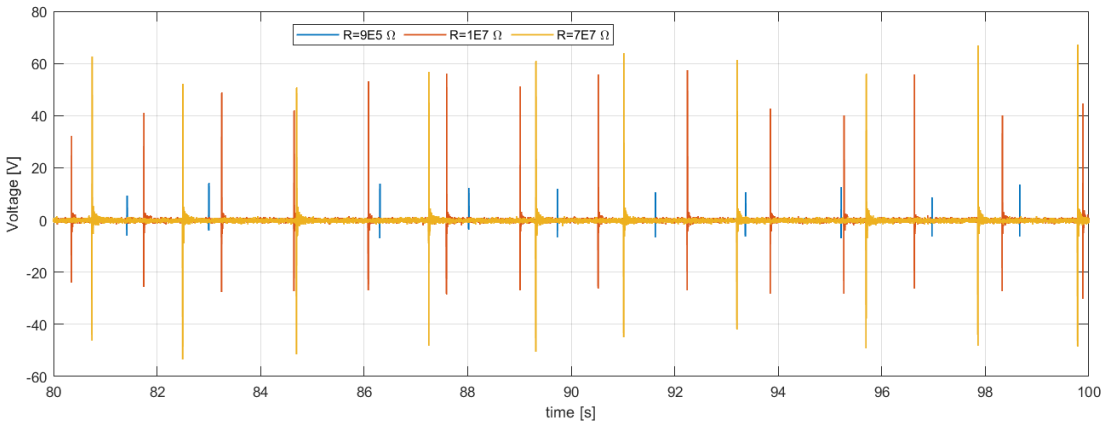

Figure A.2: Voltage hammer measurements changing the resistance

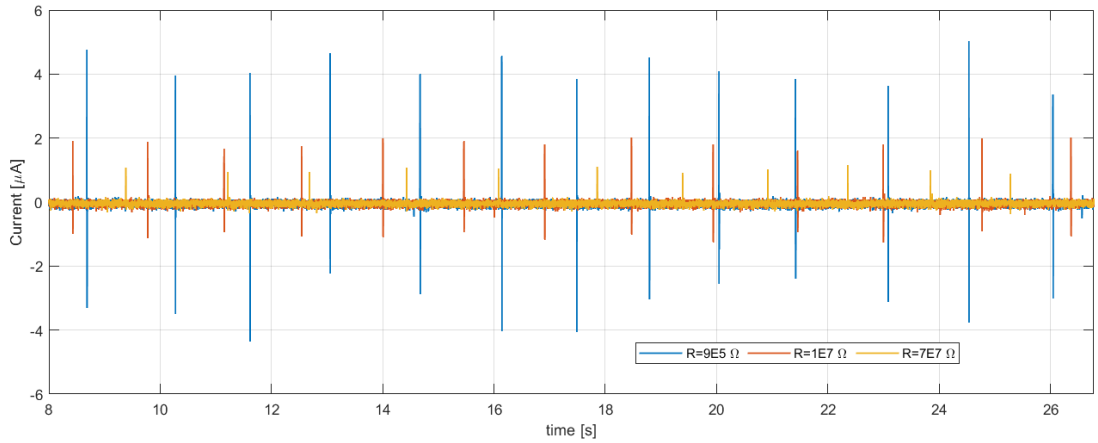

Figure A.3: Current hammer measurements changing the resistance

A.2 Nokian Tyres Experiments

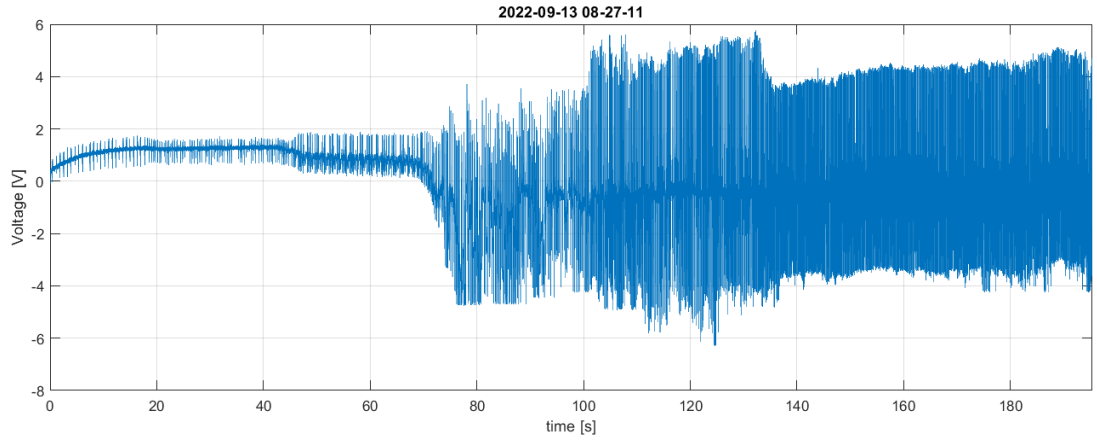

Figure A.4: Voltage measurements from the nokian test

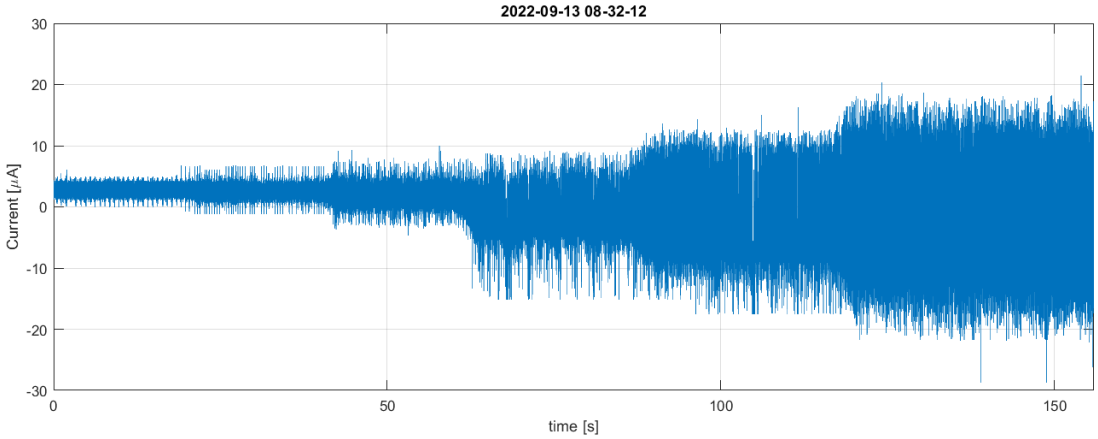

Figure A.5: Current measurements from the nokian test